12-2017

Description and Practical Application of the Physiologic Distribution of 3'-Deoxy-3'-[18F]Fluorothymidine in Companion Animals

Joshua Alan Rowe
University of Tennessee, Knoxville, jrowe5@vols.utk.edu

To the Graduate Council:

I am submitting herewith a dissertation written by Joshua Alan Rowe entitled "Description and Practical Application of the Physiologic Distribution of 3’-Deoxy-3’-[18F]Fluorothymidine in Companion Animals." I have examined the final electronic copy of this dissertation for form and content and recommend that it be accepted in partial fulfillment of the requirements for the degree of Doctor of Philosophy, with a major in Comparative and Experimental Medicine.

Robert B. Reed, Major Professor

We have read this dissertation and recommend its acceptance:

Federica Morandi, Stephen Kennel, Stephen Kania, Jon Wall

Accepted for the Council:

Dixie L. Thompson

Vice Provost and Dean of the Graduate School

(Original signatures are on file with official student records.)

Description and Practical Application of the Physiologic Distribution of 3'-Deoxy-3'-[^{18}F]Fluorothymidine in Companion Animals

A Dissertation Presented for the

Doctor of Philosophy

Degree

The University of Tennessee, Knoxville

Joshua Alan Rowe

December 2017

ABSTRACT

Access to positron emission tomography (PET), and more recently PET combined with computed tomography (PET/CT), is increasing in veterinary medicine. This molecular imaging technology allows clinicians to map biological functions within patients based on the distribution and selective uptake of specialized positron-emitting radiopharmaceuticals. Although most clinical studies utilize 2-deoxy-2-[^{18}F]fluoro-D-glucose (^{18}FDG), a versatile but relatively nonspecific tracer that interrogates the energy metabolism of tissues, there is a growing need to establish reference values for alternative or adjunct tracers in veterinary species. Among these is 3'-deoxy-3'-[^{18}F]fluorothymidine (^{18}FLT), a thymidine analog that selectively accumulates in proliferating tissues. In the present work, ^{18}FLT distribution in clinically healthy adult dogs and young adult cats was imaged using a state-of-the-art PET/CT scanner to define normal uptake levels within numerous tissues, including major parenchymal organs, bone marrow, and other sites of increased radiopharmaceutical uptake. The marrow signal was subsequently segmented into separate skeletal regions, and used to quantitatively define the adult marrow distribution pattern in the dog. Marrow activity is concentrated in the vertebral column (particularly within the thoracic and lumbar regions), sternum, ribs, and proximal aspects of the appendicular skeleton in the adult dog. Feline marrow distribution is similar; however, considerable uptake within more distal appendicular structures suggests that age-related marrow conversion is ongoing in 3-year-old cats. Outside the marrow compartment, physiologic uptake was observed within the urinary and biliary systems, intestinal tract, and variably within lymphoid structures. Prominent uptake within the hepatic parenchyma was also observed in cats,

but not dogs, at the times imaged in this study. The details of normal canine and feline ^{18}FLT biodistribution included in this dissertation may be used to inform lesion interpretation in dogs and cats with suspected disease. Likewise, quantitative details of adult marrow distribution in dogs may be used by clinicians to guide the selection of marrow sampling sites or inform tissue-sparing efforts during radiotherapeutic planning in canine patients.

TABLE OF CONTENTS

INTRODUCTION 1

Basic Historical and Technical Aspects of Positron Emission Tomography (PET) 2

Current Status and Limitations of 2-deoxy-2-[^{18}F]fluoro-D-glucose (^{18}FDG) 6

3'-deoxy-3'-[^{18}F]Fluorothymidine (^{18}FLT) as a Proliferation Tracer 7

Physiologic Distribution and Metabolism of ^{18}FLT 9

Bone Marrow Assessment Using ^{18}FLT 11

^{18}FLT-PET in Veterinary Medicine 12

Quantifying Uptake in PET Images 13

References 15

PART 1: WHOLE-BODY BIODISTRIBUTION OF 3'-DEOXY-3'-[^{18}F]FLUOROTHYMIDINE (^{18}FLT) IN HEALTHY ADULT CATS 32

Abstract 33

Introduction 34

Methods 36

Results 39

Discussion 40

References 46

Appendix 53

PART 2: WHOLE-BODY BIODISTRIBUTION OF 3'-DEOXY-3'-[^{18}F]FLUOROTHYMIDINE (^{18}FLT) IN HEALTHY ADULT DOGS 58

Abstract 59

Introduction 60

Methods 61

Results 64

Discussion 66

References 71

Appendix 79

PART 3: RELATIVE SKELETAL DISTRIBUTION OF PROLIFERATING MARROW IN THE ADULT DOG DETERMINED USING ^{18}FLT-PET/CT IMAGING 84

Abstract 85

Introduction 86

Methods 88

Results 90

Discussion 91

References 95

Appendix 101

CONCLUSION 106

VITA 108

LIST OF TABLES

Table 1.1 Mean and maximum standardized uptake values of ^{18}FLT uptake measured with positron emission tomography/computed tomography for selected regions in healthy, young adult cats (n=6) 54

Table 2.1 Mean and maximum standardized uptake values of ^{18}FLT uptake measured with positron emission tomography/computed tomography for selected regions in healthy, adult dogs (n=6).....80

Table 3.1 Percentage of canine total bone marrow activity by skeletal site..... 102

LIST OF FIGURES

Figure 1.1 Fused positron emission tomography/computed tomography (PET/CT) images depicting how regions of interest (ROIs) were drawn for cats.....55

Figure 1.2 Representative images illustrating ^{18}FLT whole-body biodistribution patterns observed in healthy young adult cats at 80.83 ± 7.52 (mean±SD) minutes post-injection.....56

Figure 1.3 Oblique 3-dimensional fused positron emission tomography/computed tomography images highlighting ^{18}FLT uptake within feline hematopoietic bone marrow.....57

Figure 2.1 Fused positron emission tomography/computed tomography (PET/CT) images depicting selected regions of interest (ROI) used to measure biodistribution in dogs.....81

Figure 2.2 Representative images illustrating ^{18}FLT whole-body biodistribution patterns observed in healthy adult dogs at 77.10 ± 12.83 minutes (mean±SD) minutes post-injection.....82

Figure 2.3 Focal site of presumed splenic extramedullary hematopoiesis in one dog.....83

Figure 3.1 Sagittal plane image depicting canine vertebral column regions of interest..... 103

Figure 3.2 Box plots showing percentage distribution of proliferative bone marrow by skeletal site in the adult dog (n = 6) 104

Figure 3.3 Three-dimensionally reconstructed image of canine skeletal marrow activity 105

INTRODUCTION

Basic Historical and Technical Aspects of Positron Emission Tomography (PET)

Functional imaging utilizing PET technology has played an increasingly important role in the management of human diseases in the past several decades [1-3]. Although the technology has existed since the 1960s [4], it was the late 1970s and 1980s when clinical interest began to develop around its use. Early reports predominately describe use in brain and cardiac disorders [4, 5]. At present, however, a PubMed search for "positron emission tomography" will yield over 70,000 results covering a broad range of applications ranging from psychiatry to oncology. The breadth of possible applications relates to the core functional element of PET, the radiopharmaceutical.

A PET radiopharmaceutical represents the coupling of two distinct functional components: a molecular vehicle that drives distribution within the patient and a positron-emitting radionuclide that allows that distribution to be detected, imaged, and quantified [6, 7]. The pharmaceutical vehicle may interact with a patient's body through any of a variety of biologic processes in order to drive distribution of the tracer. Examples include cell surface interactions such as antigen–antibody coupling or receptor binding, acting as substrates for enzymes or transporters, or participating directly in metabolic processes [6]. Ultimately, selection of the pharmaceutical vehicle depends on the physiologic process that is being investigated. Although the radionuclide serves predominately as a label for detection, its selection must balance availability, practicality, and any potential impacts on the functional characteristics of the radiopharmaceutical. There are several positron-emitting radionuclides from which to choose (^{15}O, ^{13}N, ^{11}C, ^{18}F, ^{68}Ga, and a few others); however, ^{18}F is used most

commonly in the clinical setting due to its ability to be substituted into a number of biologically relevant molecules, manageable effects on biochemical characteristics, favorable imaging characteristics, and convenient half-life of 109.8 minutes [6, 7].

Detection and localization of tracer distribution is possible due to the unique physical properties of positron emission. When a positron-emitting radionuclide decays by transmutation of a proton to a neutron with the corresponding release of an electron neutrino, and more importantly, a positron (essentially a “positive electron”), that positron travels only a short distance before effectively running out of energy and annihilating with an electron from the surrounding tissue [7-9]. The distance traveled by the positron depends on the energy with which it is emitted, a characteristic of the particular isotope. For ^{18}F (with an E_{max} of 633 keV), that range is around 0.6 mm on average [7]. The annihilation event results in the conversion of the masses of the two particles to a pair of characteristic 511 keV gamma rays, released almost exactly 180º apart. Ideally, these photons will strike opposing detectors of the PET camera in coincidence, allowing recovery of the location of the annihilation event along a line of response (LOR) connecting the detectors – a so-called “true” coincidence event. Each paired event is stored within the computer and used to reconstruct the distribution of the radioactivity using a reconstruction algorithm, thereby indirectly mapping the functional process being interrogated [2, 7-9].

Historically, spatial resolution has been a limitation of PET with that of early scanners exceeding 15 mm [2]. In part, this is due to intrinsic limitations imposed by the physics of positron emission. Since LORs indicate the location of the annihilation event rather

than the actual position of the tracer, positron range inherently degrades spatial resolution. Moreover, if the kinetic energy carried by the positron is not entirely dissipated prior to annihilation, the resultant photons will be released at an angle less than 180º to conserve that momentum and the LOR assigned by the scanner will misrepresent their origin [7, 8]. While these effects impose a lower limit on achievable spatial resolution, there are a variety of other factors that can produce more substantial influences on image quality. True coincidences represent only a fraction of the total counts detected, and not all annihilation photons will even reach the detectors due to attenuation. Scatter, whereby photons interact with the tissue and are redirected prior to reaching the detectors (albeit at some energy less than 511 keV), and random coincidences, whereby 2 photons from unrelated annihilation events happen to strike apposing detectors within the coincidence time window, both contribute to background noise and degrade image quality [7]. Fortunately, improvements in detector design and materials (resulting in faster scintillation, reduced dead time, and improved energy resolution), electronics, and reconstruction algorithms have greatly improved image quality in modern clinical scanners with typical resolutions now in the 4-5 mm range [2, 7, 10].

Fusion of PET data with computed tomography (CT) has further enhanced clinical utility. While functional PET images generally offer little morphological information, CT can provide the high-resolution anatomical detail necessary to reliably localize variations in uptake [11, 12]. Beyond visual comparison of the two modalities by the reader, spatial co-registration of both datasets has been shown to further improve lesion localization accuracy [13]. Fusion was initially performed using software-based methods to align

scans produced by separate machines; however, time progression and movement between scans (particularly that of internal organs which cannot be eliminated) often complicated the process and success was limited beyond the brain [11]. More recently, combined PET/CT scanners, introduced in the late 1990s and early 2000s, have largely solved the alignment problem and expanded the utility of PET-CT fusion [3]. Inclusion of both modalities within a single housing has allowed the scans to be performed in immediate succession with no alterations to patient position. As such, this has produced more consistent co-registration and increased efficiency, as well as a convenient opportunity for improved attenuation correction [11].

The degree to which tissues attenuate the signal from annihilation photons must be taken into account and corrections must be performed during image reconstruction to ensure the quantitative integrity of uptake data. Without attenuation correction, uptake is typically artifactually increased in the skin and lungs and non-uniform in other organs such as the liver and spleen. In order to calculate correction factors, stand-alone PET scanners require additional transmission scans with an external source of high energy photons (e.g. ^{68}Ge rods). These scans extend overall imaging time and introduce additional noise into the data since the process relies on photon counting statistics [7]. Conversely, modern PET/CT scanners are able to make use of co-registered CT data to obtain the necessary correction factors. In this context, the patient's CT scan, which can be performed in a fraction of the time needed to perform a separate PET-based transmission scan, provides what is essentially a map of attenuation coefficients at the mean CT x-ray energy (70-80 keV) [3, 7, 9, 12]. Although the data must be scaled to match the PET energy of 511 keV, CT-based correction is essentially noiseless and can

reduce scan times by more than 40% [3, 11, 12]. Accordingly, PET/CT continues to gain popularity and has become increasingly available at referral imaging facilities [2, 3, 14, 15].

Current Status and Limitations of 2-Deoxy-2-[^{18}F]Fluoro-D-Glucose (^{18}FDG)

At present, ^{18}FDG is by far the most commonly used PET tracer in the clinical setting [6]. This ^{18}F-labelled tracer is an analog of glucose that participates in the hexokinase reaction of glycolysis. The product of this reaction, ^{18}FDG-6-PO_4, is denied further metabolic progression due to the absence of a hydroxyl group at C-2 and becomes trapped within cells [16, 17]. The absence of a hydroxyl group at C-2 also prevents resorption in the renal tubule, increasing excretion of extracellular ^{18}FDG and reducing background activity. As a result, imaging ^{18}FDG distribution provides a map of tissue glycolytic activity with favorable signal-to-noise ratios for lesion detection in most tissues [17]. Human physiologic uptake normally occurs in metabolically active tissues (particularly the brain, but also skeletal muscles and myocardium under certain conditions, as well as variable uptake in lymphoid and gastrointestinal structures). Since ^{18}FDG is eliminated via the urine, intense uptake in the renal pelves, ureters, and urinary bladder is also a normal and prominent component of ^{18}FDG distribution in humans [18-23]. Similar distribution is observed in common veterinary species [24-30].

Researchers have used ^{18}FDG since the late 1970s [31] and it remains the first-line PET tracer for most clinical applications, including oncology, cardiology, and neurology [15, 32]. Since most pathologic conditions are accompanied by alterations in glucose management, ^{18}FDG is especially versatile. Unfortunately, the nonspecific nature of

altered glucose metabolism can also represent a major drawback in certain situations [6]. Although ^{18}FDG-PET is highly sensitive for detecting both primary and metastatic tumors due to their characteristic increased energy consumption, false-positive uptake is often also present in areas of infection or inflammation [23, 33, 34]. The utility of ^{18}FDG in measuring response to certain treatments, particularly those that often incite an inflammatory response, can be complicated [35, 36], and not all tumors are ^{18}FDG avid [37, 38]. Moreover, physiologic uptake in metabolically active tissues can influence ^{18}FDG's ability to discriminate lesions in these areas [18-20, 22, 23, 39]. While ^{18}FDG will likely remain the workhorse of clinical PET for the foreseeable future, there is a need for validating alternative and adjunct imaging options for applications where a traditional ^{18}FDG-PET scan is inadequate or inappropriate [40]. Direct measurement of proliferation frequently offers greater specificity than indirect measurement via energy metabolism. Consequently, radiopharmaceuticals that specifically target the pathways of DNA synthesis offer a useful alternative to characterize proliferative disorders [41].

3'-deoxy-3'-[^{18}F]Fluorothymidine (^{18}FLT) as a Proliferation Tracer

^{18}FLT, a close variant of the antiviral compound 3'-azido-3'-deoxythymidine (AZT), is the most prominent proliferation marker currently used in PET imaging [6, 42]. Both compounds are analogs of thymidine, the only nucleoside used in the production of DNA that is not also incorporated into RNA [43-45]. Structurally, ^{18}FLT differs from thymidine only by the presence of the ^{18}F-label rather than a hydroxyl group at the 3' position [46].

^{18}FLT uptake is facilitated by the pyrimidine salvage pathway, the mechanism by which thymidine and its analogs are transported into cells and phosphorylated as an initial step toward DNA synthesis [41]. Entrance into the cell is accomplished by both facilitated transport and passive diffusion [42], while phosphorylation occurs via thymidine kinase 1 (TK1) [43]. Phosphorylated ^{18}FLT is trapped intracellularly, but lacking the necessary 3'-hydroxyl, never significantly incorporated into DNA [47]. Consequently, it is phosphorylation by TK1 that forms the basis of ^{18}FLT accumulation rather than the entirety of DNA synthesis. This is very similar to the underlying mechanism of ^{18}FDG, wherein phosphorylation by hexokinase rather than progression through the entirety of glucose metabolism is responsible for tracer retention [48].

Despite not being incorporated into DNA, there are several aspects of ^{18}FLT metabolism that make it a suitable marker of proliferation. First and foremost, TK1 function is tightly regulated – activity is increased in proliferating and malignant cells but essentially absent in quiescent cells [49, 50]. Expression increases 10-fold during the synthetic phase of the cell cycle, but rapidly declines thereafter [49, 51]. Secondly, putative deoxynucleotidase-mediated dephosphorylation of ^{18}FLT-monophosphate, the product of TK1, occurs slowly. Since the cell membrane is impermeable to phosphorylated ^{18}FLT, sluggish dephosphorylation limits efflux of the tracer and allows a stable retention window for imaging [52]. Finally, unlike thymidine, ^{18}FLT is not degraded by thymidine phosphorylase (which would produce labeled metabolites) [52, 53], nor is it a substrate for thymidine kinase 2 (the isozyme involved in mitochondrial, rather than nuclear, DNA replication and repair) [54]. These factors simplify image analysis and link ^{18}FLT exclusively to nuclear DNA synthesis [41].

Oncologic imaging represents an obvious application for a tracer that measures cellular proliferation. ^{18}FLT uptake has been shown to correlate strongly with traditional measures of proliferation, including Ki-67 immunostaining, for a variety of human cancers [41, 47, 55]. Unfortunately, however, there are a number of factors that can influence ^{18}FLT uptake. It is important to consider the cell population that is being interrogated when evaluating suitability. Since it is the salvage pathway that governs retention of the tracer, factors that influence the utilization of this pathway, such as the existing cellular thymidine concentration or predilection toward the *de novo* pathway, will impact imaging performance [56, 57]. Likewise, recent administration of certain chemotherapeutic agents that cause upregulation of the salvage pathway, like 5-fluorouracil or methotrexate, may confound interpretation [58]. ^{18}FLT-based imaging often displays lower uptake levels and/or sensitivity when compared to ^{18}FDG for detecting most cancers [47, 59-66]; however, greater specificity in many applications, particularly when inflammation or lymph node involvement may be implicated, supports that there is a role for ^{18}FLT in cancer imaging [62-67]. While it is unlikely that ^{18}FLT will replace ^{18}FDG for most initial tumor detection or staging efforts, a number of recent studies have demonstrated promising results for the use of ^{18}FLT in evaluating treatment response or predicting relapse [68-73].

Physiologic Distribution and Metabolism of ^{18}FLT

Human studies have primarily demonstrated physiologic ^{18}FLT uptake in the bone marrow, liver, kidneys, and urinary bladder. Bone marrow is a known site of abundant proliferation related to blood cell production. The other organs are primarily involved in

metabolism or excretion of the tracer. Unlike ^{18}FDG, little to no uptake is seen in the brain, myocardium, or skeletal muscle [47, 74]. Preclinical work in the canine exhibited similar qualitative biodistribution to the human, although hepatic parenchymal uptake was reduced and uptake was also noted in the mandibular lymph nodes and muzzle [43]. Lymph node aspirates were not collected, but the observed lymphoid uptake may have been due to reactive B-lymphocyte proliferation within germinal centers [75].

Metabolism within the liver occurs via glucuronidation, the process by which glucuronic acid is transferred to chemical compounds to form metabolites that are more hydrophilic and readily excreted [76]. Glucuronidation is facilitated by a group of conjugative enzymes known as UDP-glucuronosyltransferases (UGTs) which originally evolved to detoxify various chemicals found in dietary plants but are now important contributors to drug metabolism [77]. The specific isozyme responsible for AZT glucuronidation in humans is UGT2B7 [78]; therefore, it is likely that this isozyme also facilitates ^{18}FLT metabolism. In the human, this process is an important contributor to ^{18}FLT kinetics, with approximately 25% of the plasma activity present as ^{18}FLT-glucuronide at 60 minutes post-injection [76]. Conversely, analyses of canine blood and urine suggest that the glucuronide pathway contributes very little to ^{18}FLT elimination in the dog and that the vast majority of ^{18}FLT is excreted unchanged [43, 79, 80]. These findings likely explain the disparity observed in hepatic uptake between the two species, and are consistent with the *in vitro* metabolism of AZT by cultured hepatocytes. This suggests glucuronidation is far more active in the livers of humans than of dogs [81].

Unfortunately, there appear to be no data available concerning the metabolic fate of ^{18}FLT or AZT in cats; however, multiple UGTs, including UGT2B7, are known to be minimally expressed or absent in the feline liver [82]. As obligate carnivores, cats likely had little need for these enzymes during their evolution, but their absence now impacts the metabolism of several pharmaceutical agents. Most notably, the prolonged clearance and remarkable sensitivity to the adverse effects of certain nonsteroidal anti-inflammatory drugs in cats is attributed to diminished glucuronidation capacity [77, 83]. It is not clear whether alternative metabolic pathways exist in cats which may impact metabolism of ^{18}FLT.

Bone Marrow Assessment Using ^{18}FLT

As a prominent feature of physiologic distribution, ^{18}FLT uptake in bone marrow has been comprehensively defined in humans [47, 74, 84]. Kinetic evaluation shows rapid early accumulation and persistent high retention of ^{18}FLT in proliferating marrow. In part, this is because the salvage pathway is particularly robust in the marrow related to the recovery of DNA lost during red blood cell enucleation [85]. As a non-invasive, whole-body means to quantitatively evaluate hematopoietic marrow, ^{18}FLT has garnered attention in human medicine not only for its ability to delineate normal active marrow sites to maximize tissue sparing during external beam radiation planning [84, 86, 87], but also for characterizing hematopoietic disorders [88-90]. Several studies have likewise utilized ^{18}FLT to illustrate the exquisite sensitivity of cycling bone marrow to radiation insult [91-94]. Irradiation of the marrow with as little as 2 Gy has been shown to visibly reduce uptake of the tracer, presumably due to cell cycle arrest, while a

fractionated dose of 10 Gy appears to have been sufficient to cause hematopoietic cell death within the radiation field [92].

Similar applications are logical and worthwhile in veterinary species. In particular, with growing veterinary access to advanced tissue-sparing radiotherapy techniques [95], comprehensive, species-specific descriptions of active marrow distribution will be increasingly relevant to veterinary clinicians concerned about inducing hematologic toxicity.

^{18}FLT-PET in Veterinary Medicine

Access to PET and PET/CT remains relatively limited in veterinary medicine, although usage in academic settings is gaining traction. In part, this is due to growing recognition that the use of advanced techniques in animals can improve not only animal health, but also that of humans through research collaborations between physicians and veterinarians [67].

Similar to human medicine, most veterinary PET imaging is performed with ^{18}FDG [15]; however, a number of investigators have begun using ^{18}FLT in recent years to image a variety of canine cancers including bronchoalveolar carcinoma [96], lymphoma [70], fibrosarcoma [97], and various sinonasal tumors [80, 98-102]. Many of these studies have focused on the utility of ^{18}FLT for measuring or predicting response to therapy with favorable results [70, 96, 97, 100, 102].

Despite growing veterinary interest, quantitative details of normal ^{18}FLT biodistribution in veterinary species remain limited in the literature [1]. Comprehensive knowledge of

normal distribution and relative uptake levels within a given species is an integral component of image interpretation as readers must be able to reliably discriminate abnormal from normal uptake within tissues [103]. Although the dog was used as a model during early *in vivo* evaluations of ^{18}FLT [43, 79], these descriptions offer few quantitative details for evaluation, not all areas of uptake visible in the included images are discussed, and image quality is considerably lower than what is possible today with modern PET/CT.

Quantifying Uptake in PET Images

Each voxel within a PET image represents the activity concentration (Bq/ml) within that volume. As a result, PET images are inherently quantitative [104]. Although clinical interpretation is often based principally on visual assessment [1], quantitative analysis can augment this process, and when scans are acquired and analyzed under standardized conditions permit more objective comparisons to be made between studies [104].

In basic terms, there are generally two approaches for quantifying uptake in PET studies – kinetic analysis and static analysis. Since kinetic approaches require dynamic imaging to be performed, which limits the field of study to a single bed position per scan, most clinical PET studies rely on the calculation of standardized uptake values (SUVs) from static images [104]. SUVs represent a “semi-quantitative” approach to analysis which normalizes activity within a region of interest (ROI) based on the dose injected and the size of the patient [105]. SUVs are most commonly calculated based on body weight (i.e. SUV = tissue concentration (Bq/ml) / (injected dose [Bq] / body weight [g]),

but lean body mass or body surface area may also be used. A value of 1.0 suggests that there is no meaningful concentration of the tracer by a given tissue, while values greater than 1.0 indicate that some mechanism of concentration is occurring [106]. SUV calculations may be based on maximum, minimum, or average tissue concentrations, but maximum values are most commonly used in lesion analysis [15].

Despite their popularity, SUVs have been criticized because they are subject to variability from a number of sources, including several patient-, protocol-, and equipment-related elements [107]. Among these elements are factors such as patient body condition, competing transport effects (e.g. competition for glucose transporters with elevated circulating glucose concentrations in the case of ^{18}FDG), dose administered, length of uptake period, ROI size and designation parameters, reconstruction method, and equipment capabilities [104, 107-109]. Nevertheless, kinetic approaches suffer from many (though not all) of the same influences, and SUVs are considered to be similarly discriminating diagnostically [105]. Regardless of method, comparisons between institutions require careful consideration of all image acquisition and analysis factors and should be approached cautiously. Although comparisons between institutions should be approached cautiously, SUVs calculated with strict adherence to data acquisition and analysis protocols can be a fairly reliable and reproducible measure of tissue uptake [104]. Accordingly, most quantitative descriptions of tracer biodistribution, at least within the veterinary literature, have utilized the SUV [24-26, 110-112].

REFERENCES

1. Lawrence J, Rohren E, Provenzale J: PET/CT today and tomorrow in veterinary cancer diagnosis and monitoring: fundamentals, early results and future perspectives. Vet Comp Oncol 8:163-187, 2010.

2. LeBlanc AK, Daniel GB: Advanced imaging for veterinary cancer patients. Vet Clin North Am Small Anim Pract 37:1059-1077; v-i, 2007.

3. Blodgett TM, Meltzer CC, Townsend DW: PET/CT: form and function. Radiology 242:360-385, 2007.

4. Hoh CK, Schiepers C, Seltzer MA, et al: PET in oncology: will it replace the other modalities? Semin Nucl Med 27:94-106, 1997.

5. Yamamoto YL, Thompson CJ, Diksic M, et al: Positron emission tomography. Neurosurg Rev 7:233-252, 1984.

6. Wadsak W, Mitterhauser M: Basics and principles of radiopharmaceuticals for PET/CT. Eur J Radiol 73:461-469, 2010.

7. Townsend DW: Physical principles and technology of clinical PET imaging. Ann Acad Med Singapore 33:133-145, 2004.

8. Blokland JA, Trindev P, Stokkel MP, et al: Positron emission tomography: a technical introduction for clinicians. Eur J Radiol 44:70-75, 2002.

9. Zanzonico P: Positron emission tomography: a review of basic principles, scanner design and performance, and current systems. Semin Nucl Med 34:87-111, 2004.

10. Jakoby BW, Bercier Y, Conti M, et al: Physical and clinical performance of the mCT time-of-flight PET/CT scanner. Phys Med Biol 56:2375-2389, 2011.

11. Townsend DW, Carney JP, Yap JT, et al: PET/CT today and tomorrow. J Nucl Med 45 Suppl 1:4S-14S, 2004.

12. Lawrence J, Rohren E, Provenzale J: PET/CT today and tomorrow in veterinary cancer diagnosis and monitoring: fundamentals, early results and future perspectives. Vet Comp Oncol 8:163-187, 2010.

13. Pelosi E, Messa C, Sironi S, et al: Value of integrated PET/CT for lesion localisation in cancer patients: a comparative study. Eur J Nucl Med Mol Imaging 31:932-939, 2004.

14. von Schulthess GK, Steinert HC, Hany TF: Integrated PET/CT: current applications and future directions. Radiology 238:405-422, 2006.

15. Randall EK: PET-Computed Tomography in Veterinary Medicine. Vet Clin North Am Small Anim Pract 46:515-533, vi, 2016.

16. Hawkins RA, Choi Y, Huang SC, et al: Quantitating tumor glucose metabolism with FDG and PET. J Nucl Med 33:339-344, 1992.

17. Fowler JS, Ido T: Initial and subsequent approach for the synthesis of ^{18}FDG. Semin Nucl Med 32:6-12, 2002.

18. Cook GJ, Fogelman I, Maisey MN: Normal physiological and benign pathological variants of 18-fluoro-2-deoxyglucose positron-emission tomography scanning: potential for error in interpretation. Semin Nucl Med 26:308-314, 1996.

19. Cook GJ, Wegner EA, Fogelman I: Pitfalls and artifacts in ^{18}FDG PET and PET/CT oncologic imaging. Semin Nucl Med 34:122-133, 2004.

20. Engel H, Steinert H, Buck A, et al: Whole-body PET: physiological and artifactual fluorodeoxyglucose accumulations. J Nucl Med 37:441-446, 1996.

21. Ramos CD, Erdi YE, Gonen M, et al: FDG-PET standardized uptake values in normal anatomical structures using iterative reconstruction segmented attenuation correction and filtered back-projection. Eur J Nucl Med 28:155-164, 2001.

22. Abouzied MM, Crawford ES, Nabi HA: ^{18}F-FDG imaging: pitfalls and artifacts. J Nucl Med Technol 33:145-155; quiz 162-143, 2005.

23. Shreve PD, Anzai Y, Wahl RL: Pitfalls in oncologic diagnosis with FDG PET imaging: physiologic and benign variants. Radiographics 19:61-77; quiz 150-151, 1999.

24. Leblanc AK, Jakoby B, Townsend DW, et al: Thoracic and abdominal organ uptake of 2-deoxy-2-[^{18}F]fluoro-d-glucose (^{18}FDG) with positron emission tomography in the normal dog. Veterinary Radiology & Ultrasound 49:182-188, 2008.

25. Leblanc AK, Wall JS, Morandi F, et al: Normal Thoracic and Abdominal Distribution of 2-deoxy-2[^{18}F]fluoro-d-glucose (^{18}FDG) in Adult Cats. Veterinary Radiology & Ultrasound 50:436-441, 2009.

26. Lee M-S, Lee A-R, Jung M-A, et al: Characterization of Physiologic ^{18}f-Fdg Uptake with Pet-Ct in Dogs. Veterinary Radiology & Ultrasound 51:670-673, 2010.

27. Irimajiri M, Miller MA, Green MA, et al: Cerebral metabolism in dogs assessed by (18)F-FDG PET: a pilot study to understand physiological changes in behavioral disorders in dogs. J Vet Med Sci 72:1-6, 2010.

28. Hansen AE, McEvoy F, Engelholm SA, et al: FDG PET/CT imaging in canine cancer patients. Vet Radiol Ultrasound 52:201-206, 2011.

29. Kang BT, Son YD, Lee SR, et al: FDG uptake of normal canine brain assessed by high-resolution research tomography-positron emission tomography and 7 T-magnetic resonance imaging. J Vet Med Sci 74:1261-1267, 2012.

30. Randall E, Loeber S, Kraft S: Physiologic variants, benign processes, and artifacts from 106 canine and feline FDG-PET/computed tomography scans. Vet Radiol Ultrasound 55:213-226, 2014.

31. Gallagher BM, Ansari A, Atkins H, et al: Radiopharmaceuticals XXVII. ^{18}F-labeled 2-deoxy-2-fluoro-d-glucose as a radiopharmaceutical for measuring regional myocardial glucose metabolism in vivo: tissue distribution and imaging studies in animals. J Nucl Med 18:990-996, 1977.

32. Hoh CK: Clinical use of FDG PET. Nucl Med Biol 34:737-742, 2007.

33. Strauss LG: Fluorine-18 deoxyglucose and false-positive results: a major problem in the diagnostics of oncological patients. Eur J Nucl Med 23:1409-1415, 1996.

34. Metser U, Even-Sapir E: Increased (18)F-fluorodeoxyglucose uptake in benign, nonphysiologic lesions found on whole-body positron emission tomography/computed tomography (PET/CT): accumulated data from four years of experience with PET/CT. Semin Nucl Med 37:206-222, 2007.

35. Spence AM, Muzi M, Graham MM, et al: 2-[(18)F]Fluoro-2-deoxyglucose and glucose uptake in malignant gliomas before and after radiotherapy: correlation with outcome. Clin Cancer Res 8:971-979, 2002.

36. Hicks RJ: The role of PET in monitoring therapy. Cancer Imaging 5:51-57, 2005.

37. Hoh CK, Seltzer MA, Franklin J, et al: Positron emission tomography in urological oncology. J Urol 159:347-356, 1998.

38. Khan MA, Combs CS, Brunt EM, et al: Positron emission tomography scanning in the evaluation of hepatocellular carcinoma. J Hepatol 32:792-797, 2000.

39. Britton T, Robinson N: Pitfalls and Pearls of Wisdom in ^{18}F-FDG PET Imaging of Tumors. J Nucl Med Technol 44:59-64, 2016.

40. Mankoff DA, Eary JF, Link JM, et al: Tumor-Specific Positron Emission Tomography Imaging in Patients: [^{18}F] Fluorodeoxyglucose and Beyond. Clinical Cancer Research 13:3460-3469, 2007.

41. Salskov A, Tammisetti VS, Grierson J, et al: FLT: Measuring Tumor Cell Proliferation In Vivo With Positron Emission Tomography and 3′-Deoxy-3′-[^{18}F]Fluorothymidine. Seminars in Nuclear Medicine 37:429-439, 2007.

42. Kong XB, Zhu QY, Vidal PM, et al: Comparisons of anti-human immunodeficiency virus activities, cellular transport, and plasma and intracellular pharmacokinetics of 3'-fluoro-3'-deoxythymidine and 3'-azido-3'-deoxythymidine. Antimicrob Agents Chemother 36:808-818, 1992.

43. Shields AF, Grierson JR, Dohmen BM, et al: Imaging proliferation in vivo with [F-18]FLT and positron emission tomography. Nat Med 4:1334-1336, 1998.

44. Vallabhajosula S: (18)F-labeled positron emission tomographic radiopharmaceuticals in oncology: an overview of radiochemistry and mechanisms of tumor localization. Semin Nucl Med 37:400-419, 2007.

45. Cleaver JE: The relationship between the rate of DNA synthesis and its inhibition by ultraviolet light in mammalian cells. Radiat Res 30:795-810, 1967.

46. Grierson JR, Shields AF: Radiosynthesis of 3'-deoxy-3'-[(18)F]fluorothymidine: [(18)F]FLT for imaging of cellular proliferation in vivo. Nucl Med Biol 27:143-156, 2000.

47. Been LB, Suurmeijer AJ, Cobben DC, et al: [^{18}F]FLT-PET in oncology: current status and opportunities. Eur J Nucl Med Mol Imaging 31:1659-1672, 2004.

48. Shields AF: PET imaging with ^{18}F-FLT and thymidine analogs: promise and pitfalls. J Nucl Med 44:1432-1434, 2003.

49. Munch-Petersen B, Cloos L, Jensen HK, et al: Human thymidine kinase 1. Regulation in normal and malignant cells. Adv Enzyme Regul 35:69-89, 1995.

50. Boothman DA, Davis TW, Sahijdak WM: Enhanced expression of thymidine kinase in human cells following ionizing radiation. Int J Radiat Oncol Biol Phys 30:391-398, 1994.

51. Sherley JL, Kelly TJ: Regulation of human thymidine kinase during the cell cycle. J Biol Chem 263:8350-8358, 1988.

52. Grierson JR, Schwartz JL, Muzi M, et al: Metabolism of 3'-deoxy-3'-[F-18]fluorothymidine in proliferating A549 cells: validations for positron emission tomography. Nucl Med Biol 31:829-837, 2004.

53. Lee SJ, Yeo JS, Lee HJ, et al: Thymidine phosphorylase influences [(18)F]fluorothymidine uptake in cancer cells and patients with non-small cell lung cancer. Eur J Nucl Med Mol Imaging 41:1327-1335, 2014.

54. Munch-Petersen B, Cloos L, Tyrsted G, et al: Diverging substrate specificity of pure human thymidine kinases 1 and 2 against antiviral dideoxynucleosides. J Biol Chem 266:9032-9038, 1991.

55. Chalkidou A, Landau DB, Odell EW, et al: Correlation between Ki-67 immunohistochemistry and ^{18}F-fluorothymidine uptake in patients with cancer: A systematic review and meta-analysis. Eur J Cancer 48:3499-3513, 2012.

56. Zhang CC, Yan Z, Li W, et al: [(18)F]FLT-PET imaging does not always "light up" proliferating tumor cells. Clin Cancer Res 18:1303-1312, 2012.

57. McKinley ET, Ayers GD, Smith RA, et al: Limits of [^{18}F]-FLT PET as a biomarker of proliferation in oncology. PLoS One 8:e58938, 2013.

58. Dittmann H, Dohmen BM, Kehlbach R, et al: Early changes in [^{18}F]FLT uptake after chemotherapy: an experimental study. Eur J Nucl Med Mol Imaging 29:1462-1469, 2002.

59. Cobben DC, van der Laan BF, Maas B, et al: ^{18}F-FLT PET for visualization of laryngeal cancer: comparison with ^{18}F-FDG PET. J Nucl Med 45:226-231, 2004.

60. Smyczek-Gargya B, Fersis N, Dittmann H, et al: PET with [^{18}F]fluorothymidine for imaging of primary breast cancer: a pilot study. Eur J Nucl Med Mol Imaging 31:720-724, 2004.

61. Francis DL, Visvikis D, Costa DC, et al: Potential impact of [^{18}F]3'-deoxy-3'-fluorothymidine versus [^{18}F]fluoro-2-deoxy-D-glucose in positron emission tomography for colorectal cancer. Eur J Nucl Med Mol Imaging 30:988-994, 2003.

62. van Westreenen HL, Cobben DC, Jager PL, et al: Comparison of ^{18}F-FLT PET and ^{18}F-FDG PET in esophageal cancer. J Nucl Med 46:400-404, 2005.

63. Buck AK, Halter G, Schirrmeister H, et al: Imaging proliferation in lung tumors with PET: ^{18}F-FLT versus ^{18}F-FDG. J Nucl Med 44:1426-1431, 2003.

64. van Waarde A, Cobben DC, Suurmeijer AJ, et al: Selectivity of ^{18}F-FLT and ^{18}F-FDG for differentiating tumor from inflammation in a rodent model. J Nucl Med 45:695-700, 2004.

65. Yap CS, Czernin J, Fishbein MC, et al: Evaluation of thoracic tumors with ^{18}F-fluorothymidine and ^{18}F-fluorodeoxyglucose-positron emission tomography. Chest 129:393-401, 2006.

66. Lee TS, Ahn SH, Moon BS, et al: Comparison of ^{18}F-FDG, ^{18}F-FET and ^{18}F-FLT for differentiation between tumor and inflammation in rats. Nucl Med Biol 36:681-686, 2009.

67. LeBlanc AK, Peremans K: PET and SPECT imaging in veterinary medicine. Semin Nucl Med 44:47-56, 2014.

68. Tehrani OS, Shields AF: PET imaging of proliferation with pyrimidines. J Nucl Med 54:903-912, 2013.

69. Barthel H, Cleij MC, Collingridge DR, et al: 3'-deoxy-3'-[^{18}F]fluorothymidine as a new marker for monitoring tumor response to antiproliferative therapy in vivo with positron emission tomography. Cancer Res 63:3791-3798, 2003.

70. Lawrence J, Vanderhoek M, Barbee D, et al: Use of 3′-Deoxy-3′-[^{18}f]Fluorothymidine Pet/Ct for Evaluating Response to Cytotoxic Chemotherapy in

Dogs with Non-Hodgkin's Lymphoma. Veterinary Radiology & Ultrasound 50:660-668, 2009.

71. Vanderhoek M, Juckett MB, Perlman SB, et al: Early assessment of treatment response in patients with AML using [(18)F]FLT PET imaging. Leuk Res 35:310-316, 2011.

72. Bollineni VR, Kramer GM, Jansma EP, et al: A systematic review on [(18)F]FLT-PET uptake as a measure of treatment response in cancer patients. Eur J Cancer 55:81-97, 2016.

73. Rapic S, Vangestel C, Verhaeghe J, et al: Evaluation of [^{18}F]Fluorothymidine as a Biomarker for Early Therapy Response in a Mouse Model of Colorectal Cancer. Mol Imaging Biol, 2016.

74. Herrmann K, Buck AK: Proliferation imaging with (1)(8)F-fluorothymidine PET/computed tomography: physiologic uptake, variants, and pitfalls. PET Clin 9:331-338, 2014.

75. Troost EG, Vogel WV, Merkx MA, et al: ^{18}F-FLT PET does not discriminate between reactive and metastatic lymph nodes in primary head and neck cancer patients. J Nucl Med 48:726-735, 2007.

76. Shields AF, Briston DA, Chandupatla S, et al: A simplified analysis of [^{18}F]3'-deoxy-3'-fluorothymidine metabolism and retention. Eur J Nucl Med Mol Imaging 32:1269-1275, 2005.

77. Shrestha B, Reed JM, Starks PT, et al: Evolution of a major drug metabolizing enzyme defect in the domestic cat and other felidae: phylogenetic timing and the role of hypercarnivory. PLoS One 6:e18046, 2011.

78. Barbier O, Turgeon D, Girard C, et al: 3'-azido-3'-deoxythimidine (AZT) is glucuronidated by human UDP-glucuronosyltransferase 2B7 (UGT2B7). Drug Metab Dispos 28:497-502, 2000.

79. Shields AF, Grierson JR, Muzik O, et al: Kinetics of 3'-deoxy-3'-[F-18]fluorothymidine uptake and retention in dogs. Mol Imaging Biol 4:83-89, 2002.

80. Simoncic U, Jeraj R: Heterogeneity in stabilization phenomena in FLT PET images of canines. Phys Med Biol 59:7937-7955, 2014.

81. Nicolas F, De Sousa G, Thomas P, et al: Comparative metabolism of 3'-azido-3'-deoxythymidine in cultured hepatocytes from rats, dogs, monkeys, and humans. Drug Metab Dispos 23:308-313, 1995.

82. van Beusekom CD, Fink-Gremmels J, Schrickx JA: Comparing the glucuronidation capacity of the feline liver with substrate-specific glucuronidation in dogs. J Vet Pharmacol Ther 37:18-24, 2014.

83. Lascelles BD, Court MH, Hardie EM, et al: Nonsteroidal anti-inflammatory drugs in cats: a review. Vet Anaesth Analg 34:228-250, 2007.

84. Hayman JA, Callahan JW, Herschtal A, et al: Distribution of proliferating bone marrow in adult cancer patients determined using FLT-PET imaging. Int J Radiat Oncol Biol Phys 79:847-852, 2011.

85. Muzi M, Vesselle H, Grierson JR, et al: Kinetic analysis of 3'-deoxy-3'-fluorothymidine PET studies: validation studies in patients with lung cancer. J Nucl Med 46:274-282, 2005.

86. McGuire SM, Menda Y, Ponto LL, et al: A methodology for incorporating functional bone marrow sparing in IMRT planning for pelvic radiation therapy. Radiother Oncol 99:49-54, 2011.

87. McGuire SM, Bhatia SK, Sun W, et al: Using [^{18}F]Fluorothymidine Imaged With Positron Emission Tomography to Quantify and Reduce Hematologic Toxicity Due to Chemoradiation Therapy for Pelvic Cancer Patients. Int J Radiat Oncol Biol Phys, 2016.

88. Agool A, Schot BW, Jager PL, et al: ^{18}F-FLT PET in hematologic disorders: a novel technique to analyze the bone marrow compartment. J Nucl Med 47:1592-1598, 2006.

89. Agool A, Slart RH, Kluin PM, et al: F-18 FLT PET: a noninvasive diagnostic tool for visualization of the bone marrow compartment in patients with aplastic anemia: a pilot study. Clin Nucl Med 36:286-289, 2011.

90. Buck AK, Bommer M, Juweid ME, et al: First demonstration of leukemia imaging with the proliferation marker ^{18}F-fluorodeoxythymidine. J Nucl Med 49:1756-1762, 2008.

91. Koizumi M, Saga T, Inubushi M, et al: Uptake decrease of proliferative PET tracer ^{18}FLT in bone marrow after carbon ion therapy in lung cancer. Mol Imaging Biol 13:577-582, 2011.

92. Everitt S, Hicks RJ, Ball D, et al: Imaging Cellular Proliferation During Chemo-Radiotherapy: A Pilot Study of Serial ^{18}F-FLT Positron Emission Tomography/Computed Tomography Imaging for Non–Small-Cell Lung Cancer. International Journal of Radiation OncologyBiologyPhysics 75:1098-1104, 2009.

93. McGuire SM, Menda Y, Boles Ponto LL, et al: 3'-deoxy-3'-[(1)(8)F]fluorothymidine PET quantification of bone marrow response to radiation dose. Int J Radiat Oncol Biol Phys 81:888-893, 2011.

94. Menda Y, Ponto LL, Dornfeld KJ, et al: Investigation of the pharmacokinetics of 3'-deoxy-3'-[^{18}F]fluorothymidine uptake in the bone marrow before and early after initiation of chemoradiation therapy in head and neck cancer. Nucl Med Biol 37:433-438, 2010.

95. LaRue SM, Custis JT: Advances in veterinary radiation therapy: targeting tumors and improving patient comfort. Vet Clin North Am Small Anim Pract 44:909-923, 2014.

96. Ballegeer EA, Forrest LJ, Jeraj R, et al: Pet/Ct Following Intensity-Modulated Radiation Therapy for Primary Lung Tumor in a Dog. Veterinary Radiology & Ultrasound 47:228-233, 2006.

97. Zornhagen KW, Clausen MM, Hansen AE, et al: Use of Molecular Imaging Markers of Glycolysis, Hypoxia and Proliferation ((18)F-FDG, (64)Cu-ATSM and (18)F-FLT) in a Dog with Fibrosarcoma: The Importance of Individualized Treatment Planning and Monitoring. Diagnostics (Basel) 5:372-382, 2015.

98. Bowen SR, Chappell RJ, Bentzen SM, et al: Spatially resolved regression analysis of pre-treatment FDG, FLT and Cu-ATSM PET from post-treatment FDG PET: an exploratory study. Radiother Oncol 105:41-48, 2012.

99. Bradshaw T, Fu R, Bowen S, et al: Predicting location of recurrence using FDG, FLT, and Cu-ATSM PET in canine sinonasal tumors treated with radiotherapy. Phys Med Biol 60:5211-5224, 2015.

100. Bradshaw TJ, Bowen SR, Deveau MA, et al: Molecular imaging biomarkers of resistance to radiation therapy for spontaneous nasal tumors in canines. Int J Radiat Oncol Biol Phys 91:787-795, 2015.

101. Bradshaw TJ, Bowen SR, Jallow N, et al: Heterogeneity in intratumor correlations of ^{18}F-FDG, ^{18}F-FLT, and 61Cu-ATSM PET in canine sinonasal tumors. J Nucl Med 54:1931-1937, 2013.

102. Bradshaw TJ, Yip S, Jallow N, et al: Spatiotemporal stability of Cu-ATSM and FLT positron emission tomography distributions during radiation therapy. Int J Radiat Oncol Biol Phys 89:399-405, 2014.

103. Jager PL, de Korte MA, Lub-de Hooge MN, et al: Molecular imaging: what can be used today. Cancer Imaging 5 Spec No A:S27-32, 2005.

104. Weber WA: Quantitative analysis of PET studies. Radiother Oncol 96:308-310, 2010.

105. Thie JA: Understanding the standardized uptake value, its methods, and implications for usage. J Nucl Med 45:1431-1434, 2004.

106. Weissleder R, ebrary Inc.: Molecular imaging principles and practice, in, Vol. Shelton, Conn., People's Medical Pub. House,, 2009, pp xxii, 1357 p.

107. Keyes JW, Jr.: SUV: standard uptake or silly useless value? J Nucl Med 36:1836-1839, 1995.

108. Boellaard R, Krak NC, Hoekstra OS, et al: Effects of noise, image resolution, and ROI definition on the accuracy of standard uptake values: a simulation study. J Nucl Med 45:1519-1527, 2004.

109. Soret M, Bacharach SL, Buvat I: Partial-volume effect in PET tumor imaging. J Nucl Med 48:932-945, 2007.

110. Souza MJ, Wall JS, Stuckey A, et al: Static and dynamic (18) FDG-PET in normal hispaniolan Amazon parrots (Amazona ventralis). Vet Radiol Ultrasound 52:340-344, 2011.

111. Jones MP, Morandi F, Wall JS, et al: Distribution of 2-deoxy-2-fluoro-d-glucose in the coelom of healthy bald eagles (Haliaeetus leucocephalus). Am J Vet Res 74:426-432, 2013.

112. Browning ZS, Wilkes AA, Mackenzie DS, et al: Using PET/CT imaging to characterize ^{18} F-fluorodeoxyglucose utilization in fish. J Fish Dis, 2013.

PART 1

WHOLE-BODY BIODISTRIBUTION OF 3'-DEOXY-3'-[^{18}F]FLUOROTHYMIDINE (^{18}FLT) IN HEALTHY ADULT CATS

This part was previously published as a paper by Rowe JA, Morandi F, Wall JS, Akula M, Kennel SJ, Osborne D, Martin EB, Galyon GD, Long MJ, Stuckey AC, and Leblanc AK in Veterinary Radiology and Ultrasound:

> Rowe JA, Morandi F, Wall JS, et al: Whole-body biodistribution of 3'-deoxy-3'-[^{18}F]fluorothymidine (^{18}FLT) in healthy adult cats. Vet Radiol Ultrasound 54:299-306, 2013.

My primary contributions to this paper include (1) developing the project and getting IACUC approval in collaboration with mentor, (2) assistance with performance of the scans, anesthesia, and transport (3) image and data analysis (4) creation of figures and tables (5) most of the writing.

Abstract

Positron emission tomography/computed tomography (PET/CT) utilizing 3'-deoxy-3'-[^{18}F]fluorothymidine (^{18}FLT), a proliferation tracer, has been found to be a useful tool for characterizing neoplastic diseases and bone marrow function in humans. As PET and PET/CT imaging become increasingly available in veterinary medicine, knowledge of radiopharmaceutical biodistribution in veterinary species is needed for lesion interpretation in the clinical setting. The purpose of this study is to describe the normal biodistribution of ^{18}FLT in adult domestic cats. Imaging of six healthy adult castrated male cats was performed using a commercially available PET/CT scanner consisting of a 64-slice helical CT scanner with an integrated whole-body, high-resolution LSO PET scanner. Cats were sedated and injected intravenously with 108.60 ± 2.09 (mean±SD)

MBq of ^{18}FLT (greater than 99% radiochemical purity by HPLC). Imaging was performed in sternal recumbency under general anesthesia. Static images utilizing multiple bed positions were acquired 80.83 ± 7.52 (mean±SD) minutes post-injection. Regions of interest (ROIs) were manually drawn over major parenchymal organs and selected areas of bone marrow and increased tracer uptake. Standardized Uptake Values (SUVs) were calculated. Notable areas of uptake included hematopoietic bone marrow, intestinal tract, and the urinary and hepatobiliary systems. No appreciable uptake was observed within brain, lung, myocardium, spleen, or skeletal muscle. Findings from this study can be used as baseline data for future studies of diseases in cats.

Introduction

Positron emission tomography (PET) is a functional imaging modality widely used in human medicine for the diagnosis and management of neoplastic and nonneoplastic diseases [1]. More recently, the fusion of functional PET data (which is generally characterized by relatively low spatial resolution) with high-resolution morphologic data from computed tomography (CT) has resulted in a powerful diagnostic tool capable of precise anatomic localization of radiopharmaceutical uptake [2]. With PET and PET/CT becoming increasingly available to veterinary researchers and clinicians, knowledge of the normal biodistribution of popular radiopharmaceuticals in veterinary species is needed in order to reliably discriminate normal from abnormal uptake.

At present, 2-deoxy-2-[^{18}F]fluoro-D-glucose (^{18}FDG), a metabolic tracer which interrogates the glucose metabolism of tissues, remains the most commonly used PET

tracer in the clinical setting, regardless of species [3-5]. Although ^{18}FDG will likely remain the workhorse of clinical PET for the foreseeable future, the nonspecific nature of increased glucose consumption as an indicator of disease can make it difficult in some situations to discriminate malignancy from inflammation or to identify ^{18}FDG avid lesions within metabolically active normal tissues like the brain [6, 7].

Radiopharmaceuticals that specifically target the pathways of DNA synthesis offer a useful alternative to aid in the characterization of proliferative disorders [8]. 3'-deoxy-3'-[^{18}F]fluorothymidine (^{18}FLT) is the most prominent proliferation marker currently used in PET imaging [3, 9]. As a thymidine analog, ^{18}FLT participates directly in the salvage pathway of DNA synthesis as a substrate for thymidine kinase 1 (TK1) [9, 10]. Phosphorylation by TK1 results in ^{18}FLT becoming trapped within cells and forms the basis of ^{18}FLT-PET imaging. Although ^{18}FLT is not significantly incorporated into DNA due to the absence of a 3'-hydroxyl moiety, TK1 activity is tightly regulated throughout the cell cycle and most reports have demonstrated correlation between ^{18}FLT uptake and more traditional measures of proliferation, including Ki-67 scores [8, 10].

Numerous studies in humans have demonstrated the utility of ^{18}FLT in the diagnosis, staging, measurement of therapeutic response, and prediction of outcome in a variety of malignancies [8]. ^{18}FLT-PET has also been used to characterize proliferative bone marrow in relation to therapeutic planning [11, 12], response to insult [13-15], and hematologic disease [16-18]. Underscoring the potential for translation of this tracer into veterinary applications, early preclinical studies included normal and diseased dogs and two reports within the veterinary literature document the successful use of ^{18}FLT in dogs

to characterize neoplastic disease and assess therapeutic response [9, 19-21]. To date, however, there have been no reports detailing ^{18}FLT uptake or use in cats. The purpose of this study was to describe ^{18}FLT uptake in normal adult cats to facilitate use of ^{18}FLT-PET for future clinical applications in this species.

Methods

Six healthy adult cats were acquired from a dedicated research colony maintained through the laboratory animal facilities at the University of Tennessee. All cats were purpose-bred domestic short hair castrated males, 3 years of age, and weighed 5.59 ± 0.73 kg (mean ± SD; range 4.77 – 6.41 kg). Animals were housed in Institutional Animal Care and Use Committee (IACUC)-approved facilities throughout the study and all procedures were conducted in accordance with a University of Tennessee IACUC-approved protocol. Subjects were deemed healthy based on results of physical examination, recent hematology and clinical chemistry testing, and routine clinical history as university-housed research animals. In addition, no abnormalities were noted in any animal upon evaluation of whole-body computed tomography (CT) during the study.

^{18}FLT was synthesized through the radiopharmaceutical facilities at the University of Tennessee Graduate School of Medicine using a flow-based microfluidic chemistry system. The resultant microreactor product was purified by semi-prep high-performance liquid chromatography (HPLC) resulting in >99% radiochemically pure ^{18}FLT for injection. All doses were verified to be free of endotoxin prior to injection.

All animals were fasted for a minimum of 12 hours prior to general anesthesia for imaging. Following intravenous catheter placement, subjects were sedated with acepromazine (0.025-0.05 mg/kg) and butorphanol (0.2-0.4 mg/kg) and injected intravenously with 108.60 ± 2.09 MBq ^{18}FLT (mean ± SD). Animals were subsequently confined to a small cage for approximately 1 hour in order to allow distribution and tissue uptake of the radiopharmaceutical. Animals were then transferred to the scanner bed where general anesthesia was induced via intravenous bolus of propofol (titrated to effect; ≤ 4 mg/kg), followed by endotracheal intubation and anesthetic maintenance with inhaled isoflurane.

All cats were imaged in sternal recumbency using the same PET/CT scanner (Biograph mCT, Siemens Medical Solutions USA, Inc., Knoxville, TN). This scanner combines a 64-slice helical CT scanner with a high-resolution lutetium oxy-orthosilicate (LSO) PET scanner. The scanner incorporates a 50 cm transverse (*x-y* axes) by 21.8 cm (*z* axis) diagnostic field-of-view within the 78 cm patient bore. Whole-body, static PET/CT images were acquired 80.83 ± 7.52 (mean±SD) minutes after ^{18}FLT injection.

Following an initial topogram to define the area of interest, a CT scan was performed for attenuation correction as well as to aid in image analysis. Computed tomography scans were performed at 120 kV and 150 mAs, using the scanner's automated radiation dose reduction protocol (Care Dose™, Siemens Medical Solutions USA, Inc., Knoxville, TN) and using a 0.8 pitch and a 0.6 mm slice width. Computed tomography data were reconstructed using 5 mm and 2.5 mm slice thicknesses. Immediately following CT acquisition, a whole-body PET scan was performed with no alteration in subject

positioning. Five to 7 bed positions were necessary to encompass the entire body of the cats. Positron emission tomography data were acquired for 3 minutes per bed position with an energy window setting of 435-650 keV. Positron emission tomography data were reconstructed using the scanner's specific iterative reconstruction algorithm (TrueX algorithm, Siemens Medical Solutions USA, Inc., Knoxville, TN) with 3 iterations and 12 subsets, resulting in a reconstructed pixel size of 4.07 mm x 4.07 mm. Data were normalized and corrected for dead time, attenuation, scatter, and radioactive decay.

Regions of interest (ROIs) were manually drawn by a veterinarian trained in ROI placement and molecular image analysis over sites of clinical relevance and areas of increased tracer uptake, including major parenchymal organs and selected areas of bone marrow (Figure 1.1A-D) using dedicated analysis software (Inveon Research Workplace v3.0, Siemens Medical Solutions USA, Inc., Knoxville, TN). Most ROIs were drawn using transverse plane images; however, dorsal plane images were used for liver, renal cortices, spleen, intestine, and myocardium. Renal cortical ROIs were carefully drawn such that the renal pelvis was excluded as intense activity within the renal collecting system is associated with urinary excretion of the tracer. Large, homogeneous volumes of tissue (liver, lung, and epaxial muscle) were assessed via placement of single, spherical volumetric ROIs in a representative area. Care was taken to avoid inclusion of large airways within the lung. Standardized uptake values (SUVs) based on the mean and maximum voxel intensity values within each ROI were calculated utilizing a previously described standard formula [22]:

$$SUV = \frac{\frac{Bq}{ml} \text{ within ROI}}{\frac{\text{total Bq injected}}{\text{weight (g)}}}$$

All calculations were decay-corrected to injection time. The resultant ^{18}FLT-SUVs were categorized based on the following definitions: (1) low = maximum SUV less than 1; (2) mild = maximum SUV greater than 1 but less than 2.5; (3) moderate = maximum SUV greater than 2.5 but less than 5; (4) intense = maximum SUV 5 or greater.

Results

Mean and maximum SUVs for selected ROIs are summarized in Table 1.1. The mean SUV was not assessed for intestinal uptake due to the irregular uptake patterns. Whole-body images illustrating biodistribution patterns are provided in Figure 1.2A and B.

The greatest regional uptake values occurred in the urinary and hepatobiliary systems. Variable mild to moderate intestinal ^{18}FLT uptake was observed and included numerous focal areas of increased uptake, predominately within the small intestine. However, occasional foci of increased uptake were observed within the large intestine. It was not possible to identify a specific portion of the intestine to draw a repeatable ROI because the uptake was variably diffuse to multifocal. Therefore quantitative evaluation of intestinal uptake was limited to calculation of a maximum SUV, and this was assessed using a single dorsal plane ROI encompassing the majority of the small intestine. It was also not possible to determine whether the intestinal uptake was due to tracer accumulation within the intestinal wall, lumen, or some combination thereof.

Considerable tracer uptake within the bone marrow was observed, ranging from mild to moderate intensity (Figure 1.3A and B). The highest tracer uptake within the marrow compartment was primarily associated with the vertebral column, sternum, and proximal appendicular skeleton. Uptake within the distal aspect of the femur was also observed and was consistently among the highest intensity regions within the bone marrow. Focal marrow uptake was also observed within the regions of the external occipital protuberance, humeral condyles, and mandibular condyles in some animals. Although vertebral marrow uptake was assessed within the vertebral bodies of C6, T5, L4, and the sacrum; tracer activity was present throughout the vertebral column (excluding the caudal vertebrae).

Tracer uptake within the brain, lung, myocardium, and skeletal muscle was low. Splenic uptake was mild (maximum SUV of 1.18, mean SUV below 1).

Discussion

Physiologic uptake of ^{18}FLT in the cats of this study appeared to be greatest in the hematopoietic bone marrow, intestine, and the hepatobiliary and urinary systems. Observed uptake in these regions for normal cats should therefore be taken into consideration for future clinical applications in cats with suspected disease. Minimal uptake in the normal brain, lung, myocardium, skeletal muscle, and spleen should also be taken into consideration for future clinical studies. These general patterns were consistent with normal uptake in other species that have been previously described. Intense activity within the urinary system was most likely due to elimination of the tracer via the kidneys. Moderate uptake within the hepatic parenchyma and intense activity

within the gallbladder was unexpected and may have been caused by hepatic metabolism and biliary excretion of ^{18}FLT. The pattern of uptake in the bone marrow was expected, given that hematopoietic bone marrow is a well-known site of rapid cellular proliferation. The salvage pathway is particularly active in marrow due to the reclamation of DNA resulting from abundant red blood cell enucleation [23]. As expected in an adult animal, marrow activity in our cats was predominantly concentrated within the axial and proximal appendicular skeleton [24]. Indeed, the highest marrow SUV measurements in this study were observed within the proximal aspect of the humerus (maximum SUV = 4.85), a common site for bone marrow sample collection in veterinary species. Iliac uptake was also observed. However, measurements were higher in the caudal aspect of the body of the ilium (immediately cranial to the acetabulum) than in the wing of the ilium (maximum SUVs of 3.03 and 1.86, respectively). Interestingly, the distal femoral epiphyses had among the highest marrow uptake measurements in this study (maximum SUV = 3.80). This is in contrast to the established distribution of ^{18}FLT in humans where adult appendicular marrow uptake is limited to the ultraproximal extremity bones [16].

All cats in this study were 3 years of age, thus no assessment of age-related marrow conversion could be determined. Distribution of hematopoietic marrow varies as a function of age. Although active marrow is found throughout the skeleton of newborn mammals, it is progressively replaced by yellow or fatty marrow as the animal matures [24]. Previous studies in dogs and humans have used magnetic resonance imaging (MRI) to describe bone marrow composition. This technique has been used to describe lumbar vertebral, pelvic, and femoral marrow characteristics in the adult canine as well

as age-related marrow conversion in the canine pelvis, femur, and stifle joint [25-27]; however, no such data are available in cats. A report using T1-weighted magnetic resonance imaging has evaluated age-related marrow conversion in the human mandible. Human mandibular bone marrow conversion progresses caudally with the condyle representing the final remaining region of active hematopoietic marrow and it too disappears in adolescence [28]. Three of six cats in this study had observable tracer uptake within the mandible, each limited to a focal area within the condyle. This suggests that marrow conversion may still be taking place in 3-year-old cats. It is unknown what effects age-dependent conversions would have on the increased tracer uptake observed within the distal femora and variable uptake noted within the distal humeri. Future studies are needed in cats of varying ages, particularly older animals, in order to define differences in marrow SUVs that may be attributable to patient age.

Intestinal ^{18}FLT uptake was present in all 6 cats although uptake pattern was irregular and was typified by focal areas of increased tracer accumulation throughout the intestine. Despite CT fusion, it was not clear whether the uptake was related to the intestinal wall, lumen, or a combination of both sites. The addition of both intravenous and oral contrast media administration to the CT imaging protocol may have enabled this discrimination. Intestinal mucosa is a rapidly proliferative tissue and this most likely explains some component of the intestinal uptake of ^{18}FLT we observed in our cats. This is further supported by uptake present throughout the intestine, with scans performed on fasted animals ≤92 minutes from tracer injection.

In addition to intense uptake within the gallbladder, moderate hepatic tracer uptake was observed in all cats in this study (maximum SUV = 4.00). Previous reports concerning the metabolic fate of ^{18}FLT and/or the related compound 3'-azido-3'-deoxythymidine (AZT) have indicated that hepatic metabolism via glucuronidation occurs to a variable extent depending upon species [29]. Glucuronidation is the process by which glucuronic acid is transferred to chemical compounds resulting in metabolites that are more hydrophilic and readily excreted [30]. Strong hepatic uptake has been described as characteristic of human ^{18}FLT biodistribution while canine hepatic uptake has been found to be considerably less by comparison [9]. This relationship is consistent with kinetic studies in each species which demonstrate that, while circulating ^{18}FLT remains mostly unchanged in the dog, ^{18}FLT-glucuronide represents approximately one-fourth of the measured blood activity at 60 minutes in humans [19, 23]. Aside from phosphorylation by TK1 in the salvage pathway, glucuronidation is the only documented major metabolic consequence of ^{18}FLT [23].

Following this logic, hepatic uptake in the domestic cat would be expected to be very low. As an obligate carnivore, cats lack certain UDP-glucuronosyltransferases (UGTs), the group of hepatic enzymes responsible for facilitating glucuronidation, due to genetic mutations found throughout felidae. While these enzymes are mainly discussed in the context of synthetic drug metabolism, they likely evolved in large part to detoxify dietary chemicals encountered in plant-based diets. Since cats consume a diet composed primarily of animal matter, these evolutionary selective pressures could be altered, allowing genes which control these enzymes to become dysfunctional [30]. Diminished glucuronidation abilities are considered responsible for the prolonged clearance and

remarkable sensitivity of cats to the adverse effects of certain non-steroidal anti-inflammatory drugs [31]. Our finding of relatively high hepatic tracer uptake in the face of the poor glucuronidation capacity characteristic of cats may indicate that alternative metabolic pathways are responsible for hepatic uptake in this species. Further studies in a larger number of cats are needed to define the nature of the hepatobiliary ^{18}FLT uptake, and to characterize the metabolic fate of ^{18}FLT in this species. The presence of possible circulating metabolites may impact image analysis for future clinical patients.

Measurements of regional tracer uptake in this study were expressed using SUV. This is a semiquantitative measure derived from static images that normalizes activity within a ROI for the specific radiopharmaceutical dose administered and the individual patient's body weight. This measure is commonly used clinically because it allows multiple bed positions to be assessed simultaneously from a single PET scan performed at a fixed time post-injection [22, 32-34]. Despite widespread usage, the SUV has been scrutinized as it can be influenced by several patient, scanner, and protocol-related factors. Some important sources of variability include patient body composition, lesion size and location, equipment specifications, duration of uptake period, choice of reconstruction algorithm, and ROI designation parameters [22, 35-37]. As a result, strict standardization and protocol adherence is necessary to achieve repeatability and caution must be exercised when comparing SUV data between institutions and species [35, 38].

As veterinary clinicians and researchers continue to gain access to PET technology, availability of baseline biodistribution data in veterinary species will be critical. To the

authors' knowledge, this is the first report of ^{18}FLT imaging in the cat. This study describes the physiologic uptake pattern of ^{18}FLT in a small cohort of healthy young cats and can be used as a baseline for future clinical application and interpretation of ^{18}FLT-based imaging in this species. ^{18}FLT-PET and ^{18}FLT-PET/CT have already been used successfully in humans to diagnose, characterize, and manage a variety of neoplasms and hematopoietic disorders [8, 10-18]. Moreover, veterinary reports involving naturally occurring canine lymphoma, sarcoma, and bronchoalveolar carcinoma have demonstrated the utility of ^{18}FLT in detecting neoplastic lesions, evaluating therapeutic response, and recognizing disease recrudescence in dogs; the latter case report highlighting ^{18}FLT's usefulness as an adjunct to ^{18}FDG in the presumptive discrimination of inflammation from proliferative tumor [9, 20, 21]. Potential applications and indications for this imaging modality in the cat should mirror those described in other species with obvious relevance to the field of oncology and assessment of bone marrow proliferation. Physiologic uptake within the liver, bone marrow, urinary system, and variable uptake within the intestine may complicate detection of lesions within these tissues due to background uptake levels. Further studies are needed to describe ^{18}FLT uptake patterns in healthy cats of varying ages, determine how ^{18}FLT metabolism occurs in cats, and describe ^{18}FLT-PET/CT characteristics in cats with confirmed diseases.

REFERENCES

1. Alavi A, Kung JW, Zhuang H. Implications of PET based molecular imaging on the current and future practice of medicine. Semin Nucl Med. 2004;34: 56-69.

2. Blodgett TM, Meltzer CC, Townsend DW. PET/CT: form and function. Radiology. 2007;242: 360-385.

3. Wadsak W, Mitterhauser M. Basics and principles of radiopharmaceuticals for PET/CT. Eur J Radiol. 2010;73: 461-469.

4. Fowler JS, Ido T. Initial and subsequent approach for the synthesis of ^{18}FDG. Semin Nucl Med. 2002;32: 6-12.

5. LeBlanc AK, Daniel GB. Advanced imaging for veterinary cancer patients. Vet Clin North Am Small Anim Pract. 2007;37: 1059-1077; v-i.

6. Shreve PD, Anzai Y, Wahl RL. Pitfalls in oncologic diagnosis with FDG PET imaging: physiologic and benign variants. Radiographics. 1999;19: 61-77; quiz 150-151.

7. Cook GJ, Wegner EA, Fogelman I. Pitfalls and artifacts in ^{18}FDG PET and PET/CT oncologic imaging. Semin Nucl Med. 2004;34: 122-133.

8. Salskov A, Tammisetti VS, Grierson J, Vesselle H. FLT: Measuring tumor cell proliferation in vivo with positron emission tomography and 3′-Deoxy-3′-[^{18}F]Fluorothymidine. Semin Nucl Med. 2007;37: 429-439.

9. Shields AF, Grierson JR, Dohmen BM, Machulla HJ, Stayanoff JC, Lawhorn-Crews JM, et al. Imaging proliferation in vivo with [F-18]FLT and positron emission tomography. Nat Med. 1998;4: 1334-1336.

10. Been LB, Suurmeijer AJ, Cobben DC, Jager PL, Hoekstra HJ, Elsinga PH. [^{18}F]FLT-PET in oncology: current status and opportunities. Eur J Nucl Med Mol Imaging. 2004;31: 1659-1672.

11. Hayman JA, Callahan JW, Herschtal A, Everitt S, Binns DS, Hicks RJ, et al. Distribution of proliferating bone marrow in adult cancer patients determined using FLT-PET imaging. Int J Radiat Oncol Biol Phys. 2011;79: 847-852.

12. McGuire SM, Menda Y, Ponto LL, Gross B, Juweid M, Bayouth JE. A methodology for incorporating functional bone marrow sparing in IMRT planning for pelvic radiation therapy. Radiother Oncol. 2011;99: 49-54.

13. Everitt S, Hicks RJ, Ball D, Kron T, Schneider-Kolsky M, Walter T, et al. Imaging cellular proliferation during chemo-radiotherapy: a pilot study of serial ^{18}F-FLT positron emission tomography/computed tomography imaging for non–small-cell lung cancer. Int J Radiat Oncol Biol Phys. 2009;75: 1098-1104.

14. Koizumi M, Saga T, Inubushi M, Fukumura T, Yoshikawa K, Yamamoto N, et al. Uptake decrease of proliferative PET tracer ^{18}FLT in bone marrow after carbon ion therapy in lung cancer. Mol Imaging Biol. 2011;13: 577-582.

15. McGuire SM, Menda Y, Boles Ponto LL, Gross B, Buatti J, Bayouth JE. 3'-deoxy-3'-[^{18}F]fluorothymidine PET quantification of bone marrow response to radiation dose. Int J Radiat Oncol Biol Phys. 2011;81: 888-893.

16. Agool A, Schot BW, Jager PL, Vellenga E. ^{18}F-FLT PET in hematologic disorders: a novel technique to analyze the bone marrow compartment. J Nucl Med. 2006;47: 1592-1598.

17. Agool A, Slart RH, Kluin PM, de Wolf JT, Dierckx RA, Vellenga E. F-18 FLT PET: a noninvasive diagnostic tool for visualization of the bone marrow compartment in patients with aplastic anemia: a pilot study. Clin Nucl Med. 2011;36: 286-289.

18. Buck AK, Bommer M, Juweid ME, Glatting G, Stilgenbauer S, Mottaghy FM, et al. First demonstration of leukemia imaging with the proliferation marker ^{18}F-fluorodeoxythymidine. J Nucl Med. 2008;49: 1756-1762.

19. Shields AF, Grierson JR, Muzik O, Stayanoff JC, Lawhorn-Crews JM, Obradovich JE, et al. Kinetics of 3'-deoxy-3'-[F-18]fluorothymidine uptake and retention in dogs. Mol Imaging Biol. 2002;4: 83-89.

20. Ballegeer EA, Forrest LJ, Jeraj R, Mackie TR, Nickles RJ. PET/CT following intensity-modulated radiation therapy for primary lung tumor in a dog. Vet Radiol Ultrasound. 2006;47: 228-233.

21. Lawrence J, Vanderhoek M, Barbee D, Jeraj R, Tumas DB, Vail DM. Use of 3′-deoxy-3′-[^{18}F]fluorothymidine PET/CT for evaluating response to cytotoxic

chemotherapy in dogs with non-hodgkin's lymphoma. Vet Radiol Ultrasound. 2009;50: 660-668.

22. Weber WA. Quantitative analysis of PET studies. Radiother Oncol. 2010;96: 308-310.

23. Muzi M, Vesselle H, Grierson JR, Mankoff DA, Schmidt RA, Peterson L, et al. Kinetic analysis of 3'-deoxy-3'-fluorothymidine PET studies: validation studies in patients with lung cancer. J Nucl Med. 2005;46: 274-282.

24. Gurevitch O, Slavin S, Feldman AG. Conversion of red bone marrow into yellow - cause and mechanisms. Med hypotheses. 2007;69: 531-536.

25. Armbrust LJ, Hoskinson JJ, Biller DS, Wilkerson M. Low-field magnetic resonance imaging of bone marrow in the lumbar spine, pelvis, and femur in the adult dog. Vet Radiol Ultrasound. 2004;45: 393-401.

26. Armbrust LJ, Ostmeyer M, McMurphy R. Magnetic resonance imaging of bone marrow in the pelvis and femur of young dogs. Vet Radiol Ultrasound. 2008;49: 432-437.

27. Konar M LJ. Age-related changes in MR appearance of normal bone marrow in canine stifle joints. Abstracts from the annual conference of the European association of veterinary diagnostic imaging. Vet Radiol Ultrasound. 2004;45: 586-613.

28. Yamada M, Matsuzaka T, Uetani M, Hayashi K, Tsuji Y, Nakamura T. Normal age-related conversion of bone marrow in the mandible: MR imaging findings. AJR Am J Roentgenol. 1995;165: 1223-1228.

29. Nicolas F, De Sousa G, Thomas P, Placidi M, Lorenzon G, Rahmani R. Comparative metabolism of 3'-azido-3'-deoxythymidine in cultured hepatocytes from rats, dogs, monkeys, and humans. Drug Metab Dispos. 1995;23: 308-313.

30. Shrestha B, Reed JM, Starks PT, Kaufman GE, Goldstone JV, Roelke ME, et al. Evolution of a major drug metabolizing enzyme defect in the domestic cat and other felidae: phylogenetic timing and the role of hypercarnivory. PLoS One. 2011;6: e18046.

31. Lascelles BD, Court MH, Hardie EM, Robertson SA. Nonsteroidal anti-inflammatory drugs in cats: a review. Vet Anaesth Analg. 2007;34: 228-250.

32. Leblanc AK, Jakoby B, Townsend DW, Daniel GB. Thoracic and abdominal organ uptake of 2-deoxy-2-[^{18}F]fluoro-d-glucose (^{18}FDG) with positron emission tomography in the normal dog. Vet Radiol Ultrasound. 2008;49: 182-188.

33. Leblanc AK, Wall JS, Morandi F, Kennel SJ, Stuckey A, Jakoby B, et al. Normal thoracic and abdominal distribution of 2-deoxy-2[^{18}F]fluoro-d-glucose (^{18}FDG) in adult cats. Vet Radiol Ultrasound. 2009;50: 436-441.

34. Lee M-S, Lee A-R, Jung M-A, Lee I-H, Choi J-H, Chung H-W, et al. Characterization of physiologic ^{18}F-FDG uptake with PET-CT in dogs. Vet Radiol Ultrasound. 2010;51: 670-673.

35. Keyes JW, Jr. SUV: standard uptake or silly useless value? J Nucl Med. 1995;36: 1836-1839.

36. Westerterp M, Pruim J, Oyen W, Hoekstra O, Paans A, Visser E, et al. Quantification of FDG PET studies using standardised uptake values in multi-centre trials: effects of image reconstruction, resolution and ROI definition parameters. Eur J Nucl Med Mol Imaging. 2007;34: 392-404.

37. Jaskowiak CJ, Bianco JA, Perlman SB, Fine JP. Influence of reconstruction iterations on ^{18}F-FDG PET/CT standardized uptake values. J Nucl Med. 2005;46: 424-428.

38. Thie JA. Understanding the standardized uptake value, its methods, and implications for usage. J Nucl Med. 2004;45: 1431-1434.

APPENDIX

Table 1.1 Mean and maximum standardized uptake values of ^{18}FLT uptake measured with positron emission tomography/computed tomography for selected regions in healthy, young adult cats (n=6)

Region of Interest	SUV_{mean} mean (SD)		SUV_{max} mean (SD)	
Urinary Bladder	157.55	(55.73)	220.38	(69.14)
Gallbladder	9.62	(2.46)	11.29	(3.12)
Renal Cortex	4.33	(0.80)	6.14	(1.43)
Proximal Humerus	3.70	(0.95)	4.85	(1.39)
Liver	3.75	(0.38)	4.00	(0.44)
Distal Femur	2.79	(0.76)	3.80	(1.11)
Intestine	—		3.52	(0.71)
L4 Vertebral Body	2.50	(0.71)	3.17	(0.98)
Body of Ilium	2.73	(0.84)	3.03	(0.96)
Sacrum	2.33	(0.63)	2.94	(0.77)
Sternum	2.27	(0.69)	2.44	(0.78)
T5 Vertebral Body	1.98	(0.46)	2.24	(0.41)
Proximal Femur	1.78	(0.64)	2.01	(0.76)
Wing of Ilium	1.72	(0.31)	1.86	(0.48)
C6 Vertebral Body	1.57	(0.45)	1.75	(0.51)
Spleen	0.93	(0.13)	1.18	(0.15)
Epaxial Muscle	0.91	(0.10)	0.96	(0.11)
Myocardium	0.79	(0.10)	0.84	(0.12)
Brain	0.25	(0.06)	0.47	(0.10)
Lung	0.25	(0.04)	0.28	(0.05)

SUV, standardized uptake value; SD, standard deviation.

SUV's for all paired structure regions of interest were calculated by summing data for both left and right sides. Measurements were made 80.83 ± 7.52 (mean±SD) minutes after injection. All SUVs were decay corrected to injection time.

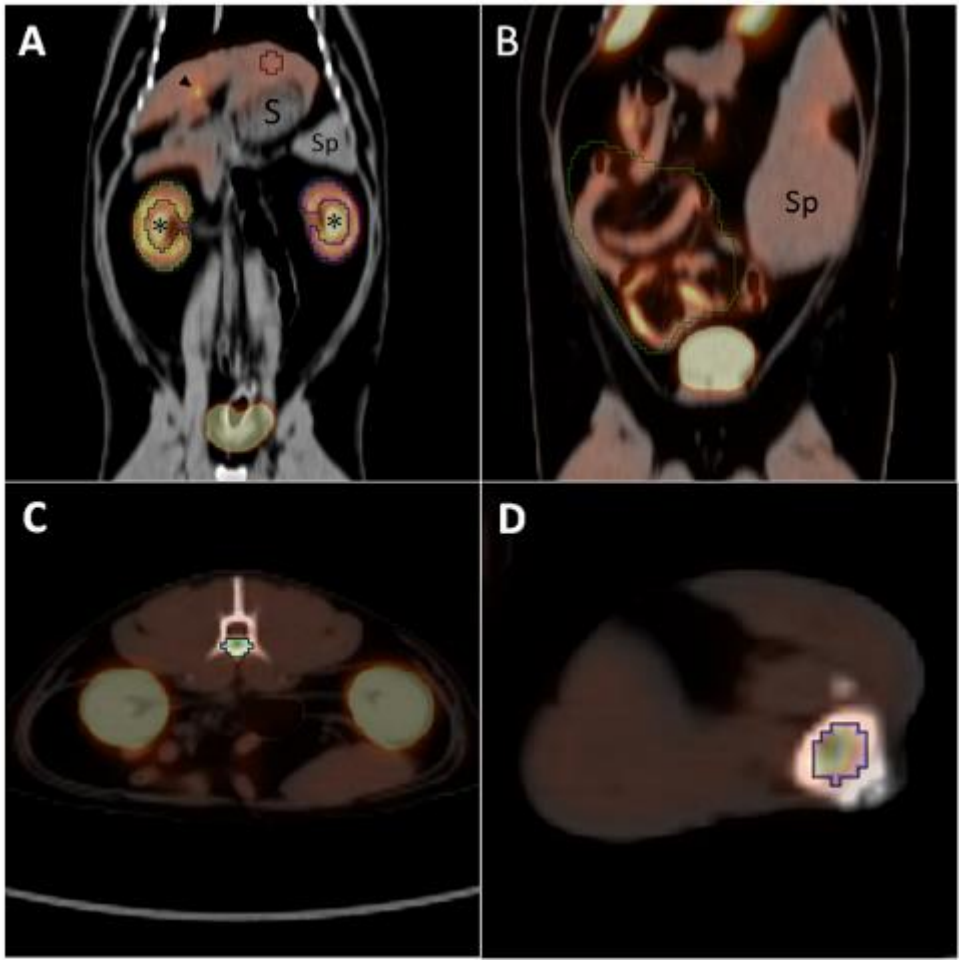

Figure 1.1 Fused positron emission tomography/computed tomography (PET/CT) images depicting how regions of interest (ROIs) were drawn for cats. (A) ROIs outlining the left (purple) and right (yellow) renal cortices were drawn to exclude the renal pelvises (asterisks) on dorsal plane images. A portion of the spherical liver ROI is outlined in red. (B) Large dorsal plane ROI outlining the small intestinal tract (green). (C) Transverse plane images were used to outline the 4th lumbar vertebral body (light blue). (D) Transverse plane ROI outlining uptake within the distal femoral epiphysis (blue). S = stomach, Sp = spleen, black arrow head = tracer uptake within gallbladder.

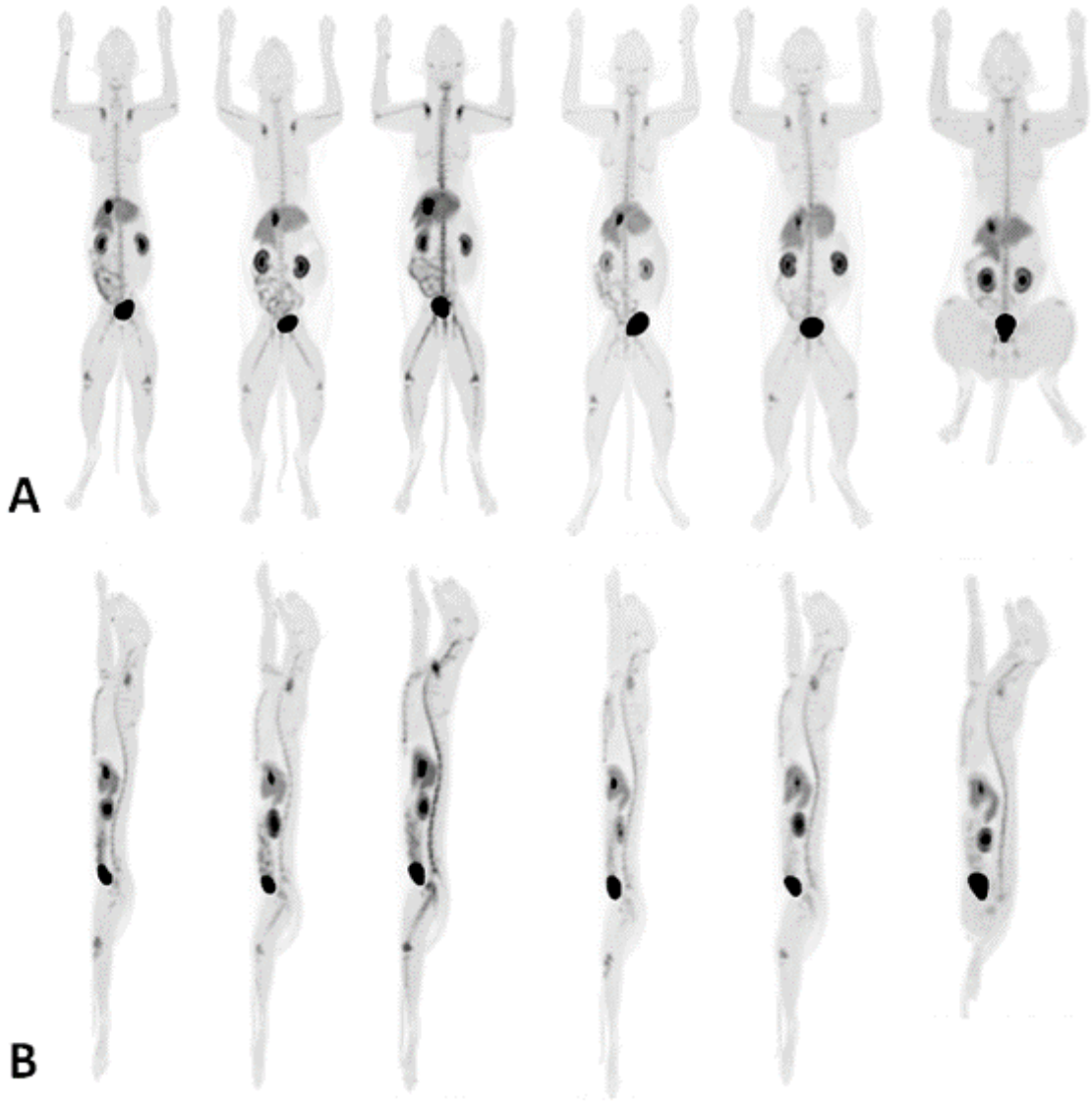

Figure 1.2 Representative images illustrating ^{18}FLT whole-body biodistribution patterns observed in healthy young adult cats at 80.83 ± 7.52 (mean±SD) minutes post-injection. Dorsal (A) and sagittal (B) plane positron emission tomography maximum intensity projections are provided. Each dorsal plane image corresponds to the sagittal plane image directly below. Image display settings are the same throughout the series.

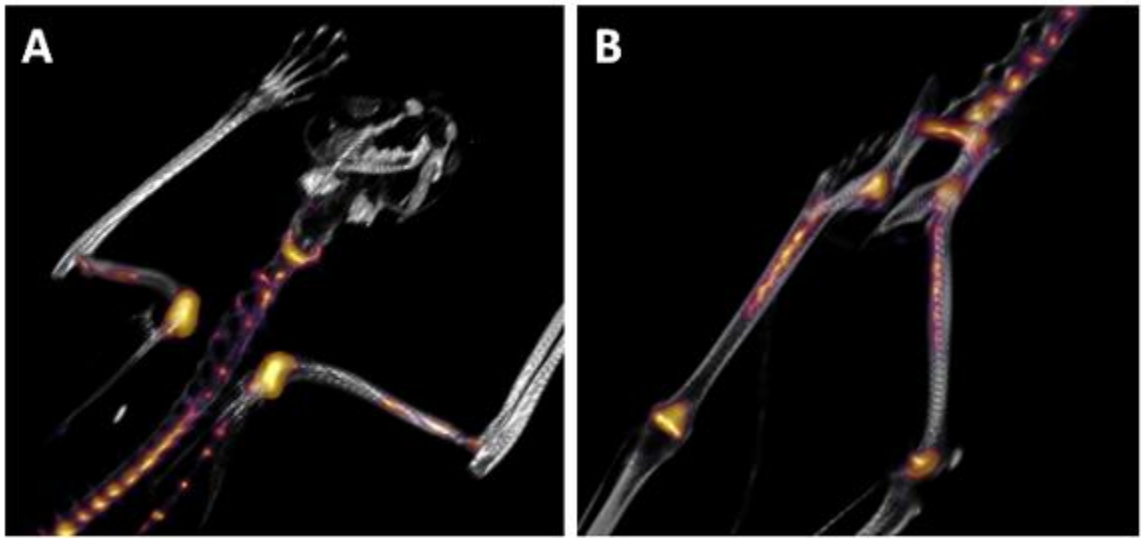

Figure 1.3 Oblique 3-dimensional fused positron emission tomography/computed tomography images highlighting ^{18}FLT uptake within feline hematopoietic bone marrow. (A) Note strong uptake within the proximal aspects of the humeri, a common marrow sampling site in the cat. Uptake is also visible within the cervical and thoracic vertebral bodies and sternum (B) Note strong uptake within the caudal aspects of the bodies of the ilia and the distal aspects of both femora. Uptake is also present within lumbar and sacral vertebral bodies.

PART 2

WHOLE-BODY BIODISTRIBUTION OF 3'-DEOXY-3'-[^{18}F]FLUOROTHYMIDINE (^{18}FLT) IN HEALTHY ADULT DOGS

This part is yet to be submitted for publication by Rowe JA, Morandi F, Wall JS, Akula M, Kennel SJ, Osborne D, Martin EB, Galyon GD, Long MJ, Stuckey AC, Reed RB, and Leblanc AK.

My primary contributions to this paper include (1) developing the project and getting IACUC approval in collaboration with mentor, (2) assistance with performance of the scans, anesthesia, and transport (3) image and data analysis (4) creation of figures and tables, (5) all of the writing.

Abstract

Positron emission tomography/computed tomography (PET/CT) utilizing 3'-deoxy-3'-[^{18}F]fluorthymidine (^{18}FLT), a marker of cellular proliferation, is increasingly recognized as a useful tool in the characterization of various cancers and bone marrow function. Although use of this technology in veterinary medicine has been limited, access to and interest in PET and PET/CT is increasing. Accordingly, detailed knowledge of the biodistribution of relevant tracers in veterinary species is required to properly interpret studies in the clinical setting. The purpose of this study is to describe the normal biodistribution of ^{18}FLT in dogs. Six healthy, adult, mixed-breed dogs were imaged utilizing a commercially available PET/CT scanner consisting of a 64-slice helical CT scanner combined with an integrated whole-body, high-resolution LSO PET scanner. Imaging was performed in sternal recumbency under general anesthesia 77.10 ± 12.83 minutes (mean±SD) after animals received an intravenous injection of 93.36 ± 41.75 MBq ^{18}FLT (mean±SD). Standardized uptake values (SUVs) were calculated based on manually drawn regions of interest (ROIs) placed over major parenchymal organs,

selected areas of bone marrow, and areas of increased tracer accumulation. Uptake was observed primarily within the urinary and biliary systems, bone marrow, and intestinal tract. Moderate uptake was variably observed in lymphoid tissues. Tracer retention in the brain, lung, myocardium, skeletal muscle, and spleen was generally low to mild, although a focal area of increased splenic uptake was observed in one animal.

Introduction

Veterinary interest in advanced imaging modalities, including positron emission tomography (PET) and combined positron emission tomography/computed tomography (PET/CT), is growing as clinicians and researchers gain access to equipment and clients increasingly demand access to care for their animals that is similar to that in human medicine [1-4]. Most PET and PET/CT studies have utilized 2-deoxy-2-[^{18}F]-fluoro-D-glucose (^{18}FDG), a radiopharmaceutical analog of glucose whose uptake reflects the energy utilization of tissues [5, 6]. The popularity of ^{18}FDG is due in large part to its versatility, as many pathological and physiological conditions are accompanied by alterations in glucose management [6]. Unfortunately, this also underlies one of the major pitfalls of this tracer, particularly in the context of oncology. It is not only tumors which accumulate the tracer, but also areas of inflammation and various normal tissues which utilize glucose to meet their energy demands [7-11]. As a result, alternative tracers must be investigated for applications where ^{18}FDG is either inappropriate or inadequate.

3'-deoxy-3'-[^{18}F]fluorothymidine (^{18}FLT) is a radiopharmaceutical analog of thymidine whose uptake and retention is more directly related to the cellular processes of

proliferation [12]. Similar to the way in which ^{18}FDG is trapped intracellularly following phosphorylation early in the glycolytic pathway, ^{18}FLT is trapped after being phosphorylated by thymidine kinase 1 (TK1) as part of the pyrimidine salvage pathway of DNA synthesis [13-15]. Although it is not ultimately incorporated into DNA as it lacks the necessary 3' hydroxyl, TK1 activity is tied closely to the cell cycle and uptake of the tracer has generally been shown to correlate favorably with traditional measures of DNA synthesis [3, 14, 16, 17].

In recent years, ^{18}FLT has become one of the most prominent of the so-called "proliferation markers", and its utility has been investigated for a broad range of human cancers in the diagnosis, staging, and/or measurement of therapeutic response [14, 18]. It has also been used as a diagnostic tool to analyze various bone marrow dyscrasias and to map normal proliferative marrow [19-24]. Although veterinary usage has been more limited to date, clinical investigations have utilized ^{18}FLT-PET in the assessment of a variety of canine cancers [2, 25-28]. Whole-body biodistribution of ^{18}FLT has been described in the cat [29] and early descriptions of physiologic ^{18}FLT distribution were based on dogs; however, comprehensive descriptions of biodistribution are still needed to aid image interpretation in this species [3, 12, 30]. The present study describes the normal distribution of ^{18}FLT in a small cohort of healthy, adult dogs.

Methods

Six healthy, purpose-bred, mixed-breed dogs were obtained through the Laboratory Animal Facilities at the University of Tennessee College of Veterinary Medicine. The study sample included 2 males (one intact, one castrated) and 4 spayed females. Age

ranged from 3 to 6 years (mean = 4.67 yrs) and weight ranged from 15.45 kg to 25.91 kg (mean = 19.09 kg). All animals were housed throughout the study in Institutional Animal Care and Use Committee (IACUC)-approved housing facilities and all procedures were conducted in compliance with a University of Tennessee IACUC-approved research protocol. Dogs were deemed to be healthy based on the results of physical examination, recent hematology and clinical chemistry testing, as well as routine history as university-maintained research animals. Additionally, no abnormalities were observed in any animal upon evaluation of whole-body computed tomography (CT) during the study.

The imaging protocol included general anesthesia for immobilization and positioning. All animals were fasted for a minimum of 12 hours prior to placement of an intravenous catheter in a peripheral vein and sedation with acepromazine (0.025-0.05 mg/kg) and butorphanol (0.2-0.4 mg/kg). At the time of sedation, animals were intravenously injected with 93.36 ± 41.75 MBq ^{18}FLT (mean±SD). The initial two study animals were administered 146.34 ± 0.26 MBq (mean ± SD) while the dosage was reduced to 66.88 ± 9.98 MBq (mean±SD) in later animals with no appreciable alteration in imaging characteristics. Following a 60-90 minute uptake period during which the animals were confined to a small cage, general anesthesia was induced via intravenous bolus of propofol (≤4 mg/kg) followed by maintenance with inhaled isoflurane.

^{18}FLT utilized in this study was produced on-site by the radiochemistry laboratory of the Molecular Imaging and Translational Research Program at the University of Tennessee Graduate School of Medicine via a flow-based microfluidic chemistry system. The

reaction product was purified by semi-prep high-performance liquid chromatography (HPLC) in order to yield >99% radiochemically pure ^{18}FLT for injection.

PET/CT imaging was performed in ventral recumbency 77.10 ± 12.83 minutes (mean±SD) after ^{18}FLT injection using a Biograph mCT scanner (Siemens Medical Solutions USA, Inc., Knoxville, TN). This scanner combines a 64-slice helical CT scanner with a high resolution LSO PET scanner within a single housing. The unit incorporates a 78 cm patient bore with a 50 cm transverse (x,y) field-of-view; the z-axis field-of-view covers 21.8 cm. CT and PET imaging were performed sequentially with no alteration in subject positioning following an initial topogram defining the area of interest. CT data were utilized for attenuation correction during PET reconstruction as well as to aid image analysis. CT scans were performed at 120 kV and 150 mAs with Care Dose™ using a 0.8 pitch and 0.6 mm acquisition slice width. CT data were later reconstructed using 5 mm and 2.5 mm slice thicknesses for image analysis. PET imaging required 9 to 11 bed positions in order to encompass the entire body of the dogs and immediately followed completion of the CT scan. PET data were acquired for 3 minutes per bed position with an energy acceptance window of 435-650 keV. PET reconstruction was performed using the TrueX algorithm (Siemens Medical Solutions USA, Inc., Knoxville, TN) with 3 iterations and 12 subsets resulting in a reconstructed pixel size of 4.07 mm x 4.07 mm. Data reconstruction included normalization and corrections for dead time, attenuation, scatter, and radioactive decay.

Regions of interest (ROIs) were manually drawn by a veterinarian trained in molecular imaging analysis over sites of observed tracer accumulation, major parenchymal

organs, and selected regions of bone marrow (Figure 2.1) using a dedicated analysis software package (Inveon Research Workplace v3.0, Siemens Medical Solutions USA, Inc., Knoxville, TN). In total, 36 separate ROIs were designated for each animal. Most regions were drawn 2-dimensionally using the imaging plane which most easily facilitated creation of a representative ROI. Large, homogeneous organs (liver, lung, urinary bladder, and epaxial muscle) were assessed via placement of individual spherical volumetric ROIs within a representative area of each tissue; care was taken to avoid large airways within the pulmonary parenchyma during placement. As urinary excretion is known to be a predominate route of ^{18}FLT elimination, renal cortical ROIs were drawn with care to exclude the renal pelvis from analysis. Mean and maximum standardized uptake values (SUVs) were calculated based on measured body weight using dedicated analysis software (Inveon Research Workplace v3.0, Siemens Medical Solutions USA, Inc., Knoxville, TN) and are decay-corrected to the time of injection. Tracer accumulation data was categorized based on the following definitions: (1) low = maximum SUV less than 1; (2) mild = maximum SUV greater than 1 but less than 3; (3) moderate = maximum SUV greater than 3 but less than 6; (4) intense = maximum SUV of 6 or greater.

Results

Biodistribution of ^{18}FLT in the canine is summarized in Table 2.1 and is greatest in the urinary and biliary systems, intestinal tract, and bone marrow. Tracer accumulation was also variably observed within lymphoid tissues. Whole-body biodistribution images are provided in Figure 2.2A and B.

The ^{18}FLT signal of greatest intensity was observed within the urinary bladder with moderate activity also present within the renal cortices. Static ^{18}FLT signal within the hepatic parenchyma was mild at the times of observation in this study; however, intense radiopharmaceutical accumulation within the gallbladder was characteristic of all dogs evaluated. Variable, multifocal to diffuse intestinal uptake was also observed, although it was not possible to discriminate tracer uptake within the intestinal wall from accumulation within the lumen.

Substantial tracer uptake within hematopoietic bone marrow was observed. All dogs in this study demonstrated similar distribution of tracer activity within the marrow compartment, with intense tracer uptake associated with the vertebral column, sternum, and proximal appendicular skeleton. Appendicular ^{18}FLT signal was consistently low to mild beyond the proximal aspect of the humerus and femur.

Lymphoid tissues also variably demonstrated radiopharmaceutical uptake in these clinically healthy animals; while uptake was mild on average, measurements in individual animals ranged from low to moderate. Although the superficial cervical and popliteal lymph nodes were the only lymphoid sites for which ROIs were designated, uptake was variably observed in other areas where lymphoid tissues are present (e.g. palatine tonsil, retropharyngeal lymph nodes). Neither aspirates nor biopsies were evaluated as a part of this study.

^{18}FLT uptake within the brain, lung, myocardium, skeletal muscle, and spleen was low to mild with the exception of a single, focal area of intense uptake (SUV = 16.6) within the spleen of one animal (Figure 2.3).

Discussion

The present study further characterizes the physiologic distribution of ^{18}FLT in the canine using PET/CT. Previous investigation in the normal dog utilizing PET without CT fusion indicated retention of the tracer in the kidneys and urinary bladder as well as selective uptake in tissues with a high proliferative rate like bone marrow. Tracer accumulation was also visualized in mandibular lymph nodes, though SUV data was not included [12]. Similar to previous findings, we observed intense physiologic uptake of ^{18}FLT within the urinary system and bone marrow. Accumulation within these tissues is a hallmark of ^{18}FLT distribution across multiple species, the former due to elimination via the urine, the latter due to the highly proliferative nature of hematopoiesis [12, 29, 30]. Additionally, we noted increased uptake within the biliary system, intestine, and variable uptake within lymphoid tissues. Observed uptake within these regions in the normal dog should therefore be considered when evaluating studies in dogs with suspected disease. Likewise, tissues which display minimal uptake – the normal brain, lung, myocardium, and skeletal muscle – should be kept in mind when considering future clinical applications. The unexpected single focus of intense uptake within the spleen of one animal is presumed to be caused by extramedullary hematopoiesis; unfortunately, samples were not collected to allow confirmation. Splenic uptake was otherwise mild in all animals suggesting that uptake in this organ is normally minimal.

Radiopharmaceutical elimination is a prominent component of the physiologic distribution of ^{18}FLT in the domestic dog with the highest uptake observed in the urinary and biliary systems. Considerable uptake within the renal cortices and urinary bladder is

expected as ^{18}FLT is cleared in large part via the urine, predominately (over 95%) as unmetabolized FLT in the canine [12]. Previous in vitro studies of the related compound, 3'-azido-3'-fluorothymidine (AZT) utilizing cultured hepatocytes support that the canine liver is responsible for very little metabolism of a similar substance [31]. This differs from humans where robust hepatic glucuronidation occurs, resulting in the presence of glucuronide-conjugates of the tracer in blood and urine [32, 33] and marked hepatic uptake [12]. The present study confirms mild hepatic tracer retention in the dog as compared to the human [12], although intense activity was present in the gallbladder. In fact, measurements within the gallbladder were consistently among the highest in this study, second only to the urinary bladder. While previous descriptions of the dog do not mention tracer accumulation within the gallbladder, an early sagittal image illustrating physiologic distribution displays a focal area of uptake in the appropriate location [12]. Further investigation evaluating bile and/or feces is needed to discern if the activity within the gallbladder is present as the parent compound or a metabolite as well as to what degree biliary excretion contributes to the distribution and elimination of the tracer.

Abundant uptake by the bone marrow is a key feature of physiologic ^{18}FLT distribution. In addition to being a site of rapid proliferation, the salvage pathway utilized by ^{18}FLT is particularly well-developed in hematopoietic marrow due to the need to recover DNA liberated during red blood cell enucleation [33]. The pattern of marrow uptake observed in these adult dogs closely mirrors that of adult humans with uptake concentrated in the vertebrae, sternum, and ultraproximal appendicular skeleton [34]. Unlike our previous observations in the young adult cat [29], discernable uptake was not present beyond the proximal aspects of the humeri or femora in any of the dogs evaluated. Conversion of

hematopoietic marrow to fat occurs with increasing age [35] and has been previously studied in the canine pelvis, femur, and stifle joint using magnetic resonance imaging (MRI). These studies suggest that conversion in the distal femur is a variable process, but likely occurs between 1 and 3 years of age in the dog [36-38]. Our findings support this assertion as conversion to an adult pattern appears to be complete in these 3-6 year old dogs.

Intestinal uptake is a frequently observed component of physiologic ^{18}FLT distribution in several species [29, 39, 40], though it has not been previously quantified in the dog. Moderate to intense intestinal uptake was present in all 6 dogs in this study. Distribution was variably multifocal to diffuse so measurements were limited to maximum SUV assessed over a large, dorsal plane ROI drawn over a representative portion of the small intestine. It is likely that intestinal uptake is the result of proliferating intestinal mucosal cells; however, given the intense uptake within the gallbladder, biliary excretion may also contribute.

Variable lymphoid uptake in these clinically healthy animals may confound interpretation of clinical studies, particularly when trying to distinguish reactive lymph nodes from lymph node metastases. Uptake within superficial cervical and popliteal lymph nodes was generally low to mild; however, moderate uptake was observed in two individuals, neither of which displayed evidence of disease based on physical examination, bloodwork, or anatomical imaging. Although other lymphoid sites were not measured in this study, modest uptake was variably present based on visual inspection and uptake within mandibular nodes has been previously reported as a component of normal

canine biodistribution [12]. Although ^{18}FLT has been shown not to accumulate in inflamed tissue since inflammatory cells are recruited from elsewhere [40, 41], interpretation of lymph node uptake is more complicated. While several groups have evaluated the specificity of ^{18}FLT for detecting lymph node metastases in a variety of cancers, results have been mixed [42-47]. Troost et al, who reported very low specificity for identifying lymph node metastases in 10 patients with head and neck cancer, determined that uptake by non-metastatic reactive lymph nodes occurs in germinal centers due to proliferating B-lymphocytes [46].

Regional uptake measurements in this study were expressed using the SUV, a semi-quantitative measure which relates uptake within an ROI to the administered radiopharmaceutical dose and patient weight. As SUVs are calculated from static images, which allow the assessment of multiple bed positions within a single study, they are a convenient and popular alternative in the clinical setting. Unfortunately, SUVs are also subject to influence by a variety of patient, equipment, and protocol-related elements beyond individual and species-specific physiologic factors. Among these are body composition, scanner specifications, image reconstruction algorithm, length of uptake period, and various aspects of the individual ROI such as size, method of placement, and whether average or maximum activity values are utilized [48-52]. SUV measurements of normal tissues in the dog are limited in the literature, but mean SUV in the vertebral marrow has been reported to be approximately 4.7 [12, 30]. While this measurement is somewhat lower than our measurements presented herein, it is difficult to compare values due to variability between studies and it is unclear specifically where previous measurements were assessed. While comparisons among species must be

approached with caution, it is interesting to note that relative to our previous description of feline ^{18}FLT biodistribution [29], which used the same scanner and protocols, canine marrow and biliary uptake is much higher, while uptake in the hepatic parenchyma, renal cortices, and urinary bladder is lower. Further investigation is required to determine the mechanisms responsible for these differences.

As PET and PET/CT continue to make inroads into veterinary medicine, detailed descriptions of normal tracer distribution in veterinary species are needed to support interpretation of studies in clinical patients. This study expands upon initial descriptions of ^{18}FLT distribution in the dog [12, 30] and provides reference data from healthy, adult animals for comparison. Further studies are needed to define the implications of biliary tracer accumulation and to validate ^{18}FLT characteristics in canine patients with confirmed disease.

REFERENCES

1. LeBlanc, A.K. and G.B. Daniel, Advanced imaging for veterinary cancer patients. Vet Clin North Am Small Anim Pract, 2007. 37(6): p. 1059-77; v-i.

2. LeBlanc, A.K. and K. Peremans, PET and SPECT imaging in veterinary medicine. Semin Nucl Med, 2014. 44(1): p. 47-56.

3. Lawrence, J., E. Rohren, and J. Provenzale, PET/CT today and tomorrow in veterinary cancer diagnosis and monitoring: fundamentals, early results and future perspectives. Vet Comp Oncol, 2010. 8(3): p. 163-87.

4. Randall, E.K., PET-Computed Tomography in Veterinary Medicine. Vet Clin North Am Small Anim Pract, 2016. 46(3): p. 515-33, vi.

5. Groves, A.M., et al., Non-[^{18}F]FDG PET in clinical oncology. Lancet Oncol, 2007. 8(9): p. 822-30.

6. Wadsak, W. and M. Mitterhauser, Basics and principles of radiopharmaceuticals for PET/CT. Eur J Radiol, 2010. 73(3): p. 461-9.

7. Abouzied, M.M., E.S. Crawford, and H.A. Nabi, ^{18}F-FDG imaging: pitfalls and artifacts. J Nucl Med Technol, 2005. 33(3): p. 145-55; quiz 162-3.

8. Engel, H., et al., Whole-body PET: physiological and artifactual fluorodeoxyglucose accumulations. J Nucl Med, 1996. 37(3): p. 441-6.

9. Shreve, P.D., Y. Anzai, and R.L. Wahl, Pitfalls in oncologic diagnosis with FDG PET imaging: physiologic and benign variants. Radiographics, 1999. 19(1): p. 61-77; quiz 150-1.

10. Cook, G.J., I. Fogelman, and M.N. Maisey, Normal physiological and benign pathological variants of 18-fluoro-2-deoxyglucose positron-emission tomography scanning: potential for error in interpretation. Semin Nucl Med, 1996. 26(4): p. 308-14.

11. Cook, G.J., E.A. Wegner, and I. Fogelman, Pitfalls and artifacts in ^{18}FDG PET and PET/CT oncologic imaging. Semin Nucl Med, 2004. 34(2): p. 122-33.

12. Shields, A.F., et al., Imaging proliferation in vivo with [F-18]FLT and positron emission tomography. Nat Med, 1998. 4(11): p. 1334-6.

13. Kong, X.B., et al., Comparisons of anti-human immunodeficiency virus activities, cellular transport, and plasma and intracellular pharmacokinetics of 3'-fluoro-3'-deoxythymidine and 3'-azido-3'-deoxythymidine. Antimicrob Agents Chemother, 1992. 36(4): p. 808-18.

14. Salskov, A., et al., FLT: Measuring Tumor Cell Proliferation In Vivo With Positron Emission Tomography and 3′-Deoxy-3′-[^{18}F]Fluorothymidine. Seminars in Nuclear Medicine, 2007. 37(6): p. 429-439.

15. Fowler, J.S. and T. Ido, Initial and subsequent approach for the synthesis of ^{18}FDG. Semin Nucl Med, 2002. 32(1): p. 6-12.

16. Vallabhajosula, S., (18)F-labeled positron emission tomographic radiopharmaceuticals in oncology: an overview of radiochemistry and mechanisms of tumor localization. Semin Nucl Med, 2007. 37(6): p. 400-19.

17. Chalkidou, A., et al., Correlation between Ki-67 immunohistochemistry and ^{18}F-fluorothymidine uptake in patients with cancer: A systematic review and meta-analysis. Eur J Cancer, 2012. 48(18): p. 3499-513.

18. Tehrani, O.S. and A.F. Shields, PET imaging of proliferation with pyrimidines. J Nucl Med, 2013. 54(6): p. 903-12.

19. Agool, A., et al., F-18 FLT PET: a noninvasive diagnostic tool for visualization of the bone marrow compartment in patients with aplastic anemia: a pilot study. Clin Nucl Med, 2011. 36(4): p. 286-9.

20. Hayman, J.A., et al., Distribution of proliferating bone marrow in adult cancer patients determined using FLT-PET imaging. Int J Radiat Oncol Biol Phys, 2011. 79(3): p. 847-52.

21. Koizumi, M., et al., Uptake decrease of proliferative PET tracer ^{18}FLT in bone marrow after carbon ion therapy in lung cancer. Mol Imaging Biol, 2011. 13(3): p. 577-82.

22. McGuire, S.M., et al., 3'-deoxy-3'-[(1)(8)F]fluorothymidine PET quantification of bone marrow response to radiation dose. Int J Radiat Oncol Biol Phys, 2011. 81(3): p. 888-93.

23. McGuire, S.M., et al., A methodology for incorporating functional bone marrow sparing in IMRT planning for pelvic radiation therapy. Radiother Oncol, 2011. 99(1): p. 49-54.

24. Wyss, J.C., et al., [(18)F]Fluoro-2-deoxy-2-d-glucose versus 3'-deoxy-3'-[(18)F]fluorothymidine for defining hematopoietically active pelvic bone marrow in gynecologic patients. Radiother Oncol, 2016. 118(1): p. 72-8.

25. Ballegeer, E.A., et al., Pet/Ct Following Intensity-Modulated Radiation Therapy for Primary Lung Tumor in a Dog. Veterinary Radiology & Ultrasound, 2006. 47(2): p. 228-233.

26. Lawrence, J., et al., Use of 3′-Deoxy-3′-[^{18}f]Fluorothymidine Pet/Ct for Evaluating Response to Cytotoxic Chemotherapy in Dogs with Non-Hodgkin's Lymphoma. Veterinary Radiology & Ultrasound, 2009. 50(6): p. 660-668.

27. Bradshaw, T.J., et al., Heterogeneity in intratumor correlations of ^{18}F-FDG, ^{18}F-FLT, and 61Cu-ATSM PET in canine sinonasal tumors. J Nucl Med, 2013. 54(11): p. 1931-7.

28. Bradshaw, T.J., et al., Spatiotemporal stability of Cu-ATSM and FLT positron emission tomography distributions during radiation therapy. Int J Radiat Oncol Biol Phys, 2014. 89(2): p. 399-405.

29. Rowe, J.A., et al., Whole-body biodistribution of 3'-deoxy-3'-[(18) f]fluorothymidine ((18) flt) in healthy adult cats. Vet Radiol Ultrasound, 2013. 54(3): p. 299-306.

30. Shields, A.F., et al., Kinetics of 3'-deoxy-3'-[F-18]fluorothymidine uptake and retention in dogs. Mol Imaging Biol, 2002. 4(1): p. 83-9.

31. Nicolas, F., et al., Comparative metabolism of 3'-azido-3'-deoxythymidine in cultured hepatocytes from rats, dogs, monkeys, and humans. Drug Metab Dispos, 1995. 23(3): p. 308-13.

32. Wagner, M., et al., 3'-[^{18}F]fluoro-3'-deoxythymidine ([^{18}F]-FLT) as positron emission tomography tracer for imaging proliferation in a murine B-Cell lymphoma model and in the human disease. Cancer Res, 2003. 63(10): p. 2681-7.

33. Muzi, M., et al., Kinetic analysis of 3'-deoxy-3'-fluorothymidine PET studies: validation studies in patients with lung cancer. J Nucl Med, 2005. 46(2): p. 274-82.

34. Agool, A., et al., ^{18}F-FLT PET in hematologic disorders: a novel technique to analyze the bone marrow compartment. J Nucl Med, 2006. 47(10): p. 1592-8.

35. Gurevitch, O., S. Slavin, and A.G. Feldman, Conversion of red bone marrow into yellow - Cause and mechanisms. Med Hypotheses, 2007. 69(3): p. 531-6.

36. Armbrust, L.J., et al., Low-field magnetic resonance imaging of bone marrow in the lumbar spine, pelvis, and femur in the adult dog. Vet Radiol Ultrasound, 2004. 45(5): p. 393-401.

37. Armbrust, L.J., M. Ostmeyer, and R. McMurphy, Magnetic resonance imaging of bone marrow in the pelvis and femur of young dogs. Vet Radiol Ultrasound, 2008. 49(5): p. 432-7.

38. Konar M, L.J., Age-related changes in MR appearance of normal bone marrow in canine stifle joints. Abstracts from the annual conference of the European

association of veterinary diagnostic imaging. Vet Radiol Ultrasound, 2004. 45(6): p. 586-613.

39. Buck, A.K., et al., Molecular imaging of proliferation in vivo: positron emission tomography with [^{18}F]fluorothymidine. Methods, 2009. 48(2): p. 205-15.

40. van Waarde, A., et al., Selectivity of ^{18}F-FLT and ^{18}F-FDG for differentiating tumor from inflammation in a rodent model. J Nucl Med, 2004. 45(4): p. 695-700.

41. Lee, T.S., et al., Comparison of ^{18}F-FDG, ^{18}F-FET and ^{18}F-FLT for differentiation between tumor and inflammation in rats. Nucl Med Biol, 2009. 36(6): p. 681-6.

42. Cobben, D.C., et al., 3'-^{18}F-fluoro-3'-deoxy-L-thymidine: a new tracer for staging metastatic melanoma? J Nucl Med, 2003. 44(12): p. 1927-32.

43. Smyczek-Gargya, B., et al., PET with [^{18}F]fluorothymidine for imaging of primary breast cancer: a pilot study. Eur J Nucl Med Mol Imaging, 2004. 31(5): p. 720-4.

44. Yap, C.S., et al., Evaluation of thoracic tumors with ^{18}F-fluorothymidine and ^{18}F-fluorodeoxyglucose-positron emission tomography. Chest, 2006. 129(2): p. 393-401.

45. Been, L.B., et al., Positron emission tomography in patients with breast cancer using (18)F-3'-deoxy-3'-fluoro-l-thymidine ((18)F-FLT)-a pilot study. Eur J Surg Oncol, 2006. 32(1): p. 39-43.

46. Troost, E.G., et al., ^{18}F-FLT PET does not discriminate between reactive and metastatic lymph nodes in primary head and neck cancer patients. J Nucl Med, 2007. 48(5): p. 726-35.

47. Hoshikawa, H., et al., Comparison of (18) F-FLT PET and (18) F-FDG PET for detection of cervical lymph node metastases in head and neck cancers. Acta Otolaryngol, 2012.

48. Keyes, J.W., Jr., SUV: standard uptake or silly useless value? J Nucl Med, 1995. 36(10): p. 1836-9.

49. Weber, W.A., Quantitative analysis of PET studies. Radiother Oncol, 2010. 96(3): p. 308-10.

50. Boellaard, R., et al., Effects of noise, image resolution, and ROI definition on the accuracy of standard uptake values: a simulation study. J Nucl Med, 2004. 45(9): p. 1519-27.

51. Kinahan, P.E. and J.W. Fletcher, Positron emission tomography-computed tomography standardized uptake values in clinical practice and assessing response to therapy. Semin Ultrasound CT MR, 2010. 31(6): p. 496-505.

52. Thie, J.A., Understanding the standardized uptake value, its methods, and implications for usage. J Nucl Med, 2004. 45(9): p. 1431-4.

APPENDIX

Table 2.1 Mean and maximum standardized uptake values of ^{18}FLT uptake measured with positron emission tomography/computed tomography for selected regions in healthy, adult dogs (n=6)

Region of Interest	SUV_{mean} mean (SD)	SUV_{max} mean (SD)
Urinary Bladder	59.65 (30.79)	100.17 (49.75)
Gallbladder	13.00 (3.75)	29.79 (11.34)
T5 Vertebral Body	7.08 (2.16)	11.10 (3.44)
L4 Vertebral Body	7.92 (2.03)	10.88 (3.08)
Proximal Humerus	5.73 (2.18)	10.66 (2.75)
Sacrum	6.80 (1.24)	10.22 (2.01)
C6 Vertebral Body	6.55 (1.12)	9.67 (1.76)
Body of Ilium	6.42 (1.33)	9.33 (1.99)
Proximal Femur	4.44 (1.53)	7.20 (2.55)
Sternum	4.07 (0.90)	6.03 (1.74)
Intestine	—	5.30 (0.84)
Wing of Ilium	3.27 (1.47)	5.03 (2.15)
Renal Cortex	2.30 (0.41)	4.83 (1.59)
Superficial Cervical LN	1.31 (1.03)	1.93 (1.70)
Popliteal LN	1.28 (0.60)	1.80 (0.88)
Mid Femur	1.37 (0.38)	1.80 (0.58)
Liver	1.60 (0.36)	1.78 (0.42)
Mid Humerus	1.43 (0.42)	1.75 (0.56)
Spleen	1.07 (0.32)	1.37 (0.43)
Distal Humerus	1.11 (0.24)	1.31 (0.28)
Myocardium	1.01 (0.24)	1.20 (0.32)
Epaxial Muscle	1.03 (0.27)	1.13 (0.28)
Distal Femur	0.30 (0.18)	0.57 (0.28)
Brain	0.29 (0.08)	0.41 (0.11)
Lung	0.28 (0.09)	0.36 (0.13)

SUV, standardized uptake value; SD, standard deviation.

SUVs for all paired structure regions of interest were calculated by summing data for both left and right sides. Measurements were made 77.10 ± 12.83 (mean±SD) minutes after injection. All SUVs were decay corrected to injection time.

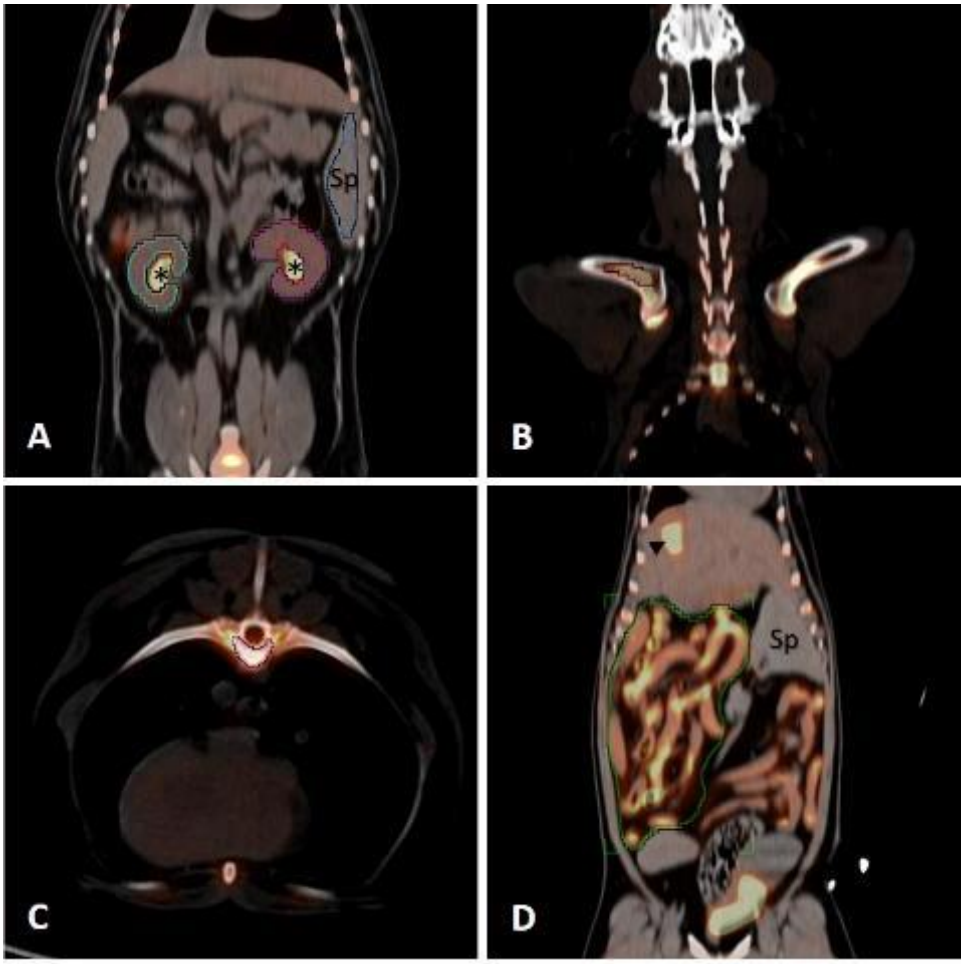

Figure 2.1 Fused positron emission tomography/computed tomography (PET/CT) images depicting selected regions of interest (ROI) used to measure biodistribution in dogs. (A) ROIs outlining the left (purple) and right (teal) renal cortices were drawn to exclude the renal pelvises (asterisks) on dorsal plane images. The splenic ROI is outlined in blue. (B) ROI outlining the right proximal aspect of the humerus drawn to approximate clinical sampling site (red). (C) Transverse plane images were used to outline the 5th thoracic vertebral body (pink). (D) Large dorsal plane ROI outlining a representative portion of the small intestine (green).

Sp = spleen, black arrowhead = tracer uptake within gallbladder

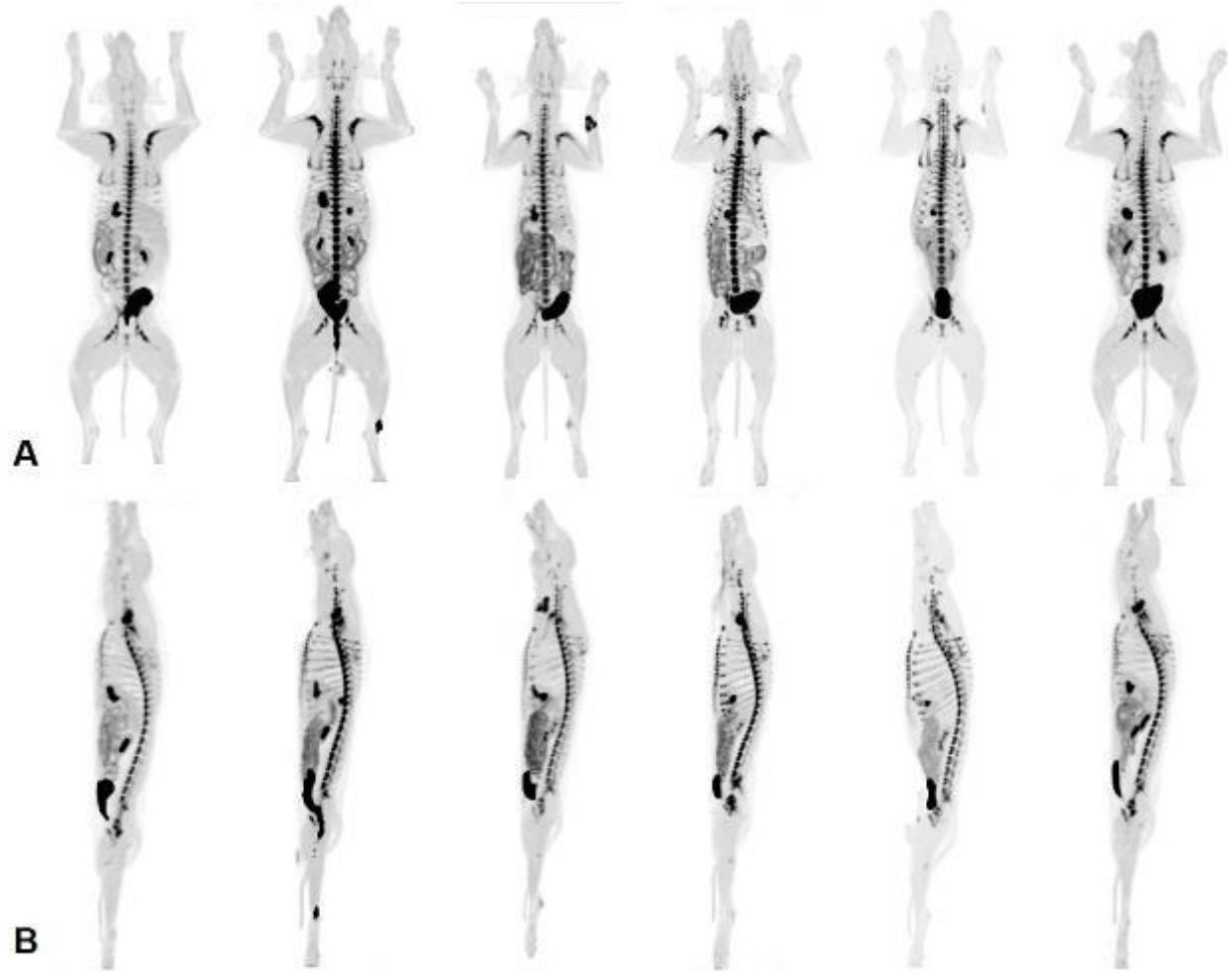

Figure 2.2 Representative images illustrating ^{18}FLT whole-body biodistribution patterns observed in healthy adult dogs at 77.10 ± 12.83 minutes (mean±SD) minutes post-injection. Dorsal (A) and sagittal (B) plane positron emission tomography maximum intensity projections are provided. Each dorsal plane image corresponds to the sagittal plane image directly below. Image display settings are the same throughout the series.

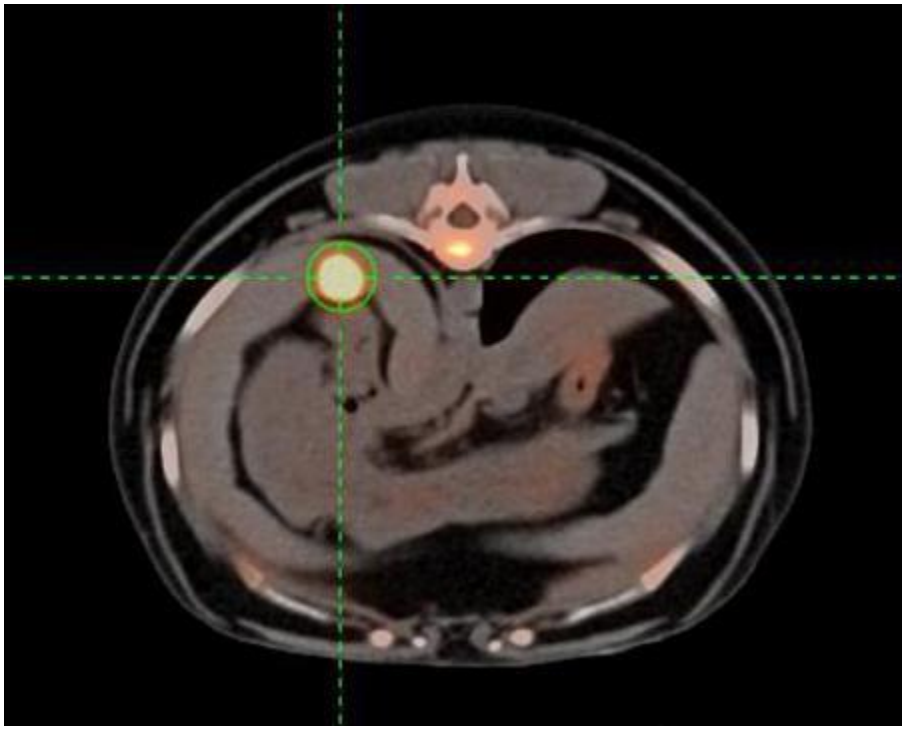

Figure 2.3 Focal site of presumed splenic extramedullary hematopoiesis in one dog.

PART 3

RELATIVE SKELETAL DISTRIBUTION OF PROLIFERATING MARROW IN THE ADULT DOG DETERMINED USING ^{18}FLT-PET/CT IMAGING

This part is yet to be submitted for publication by Rowe JA, Osborne D, Wall JS, Akula M, Kennel SJ, Galyon GD, Stuckey AC, Reed RB, and Leblanc AK.

My primary contributions to this paper include (1) developing the project, (2) image and data analysis, (3) creation of figures and tables, (4) all of the writing

Abstract

3'-deoxy-3'-[^{18}F]fluorothymidine (^{18}FLT) is a radiopharmaceutical tracer used with positron emission tomography (PET), often in combination with computed tomography (CT), to image DNA synthesis, and thus, cellular proliferation. Characteristic accumulation of the tracer within hematopoietic bone marrow provides a noninvasive means to assess marrow activity and distribution throughout the living animal. The present study utilizes three-dimensional analysis of ^{18}FLT-PET/CT scans to quantify the relative skeletal distribution of active marrow by anatomic site in the dog. Scans were performed on six healthy, adult (3 to 6 years of age), mixed-breed dogs using a commercially available PET/CT scanner consisting of a 64-slice helical CT scanner combined with an integrated whole-body, high-resolution LSO PET scanner. Regions of interest (ROIs) encompassing 11 separate skeletal regions (skull, cervical spine, thoracic spine, lumbar spine, sacrum, ribs, sternum, scapulae, proximal humeri, ossa coxarum, and proximal femora) were manually drawn based on CT images and thresholded by standardized uptake value to delineate bone marrow activity. Activity within each skeletal region was then divided by the total skeletal activity to derive the percent of overall active marrow within an individual site. The majority of active marrow was located within the vertebral column. Of the sites traditionally accessed clinically for

marrow sampling, the proximal humerus contained the largest percentage, followed by the ossa coxarum, proximal femur, and sternum, respectively. This information may be used to guide selection of traditional marrow sampling sites as well as inform efforts to spare important sites of hematopoiesis in radiation therapy planning.

Introduction

Bone marrow is a dynamic organ found throughout the skeleton within the medullary cavities of long bones and the interstices of spongy bone. In the neonate, most of the marrow is active and functions in the formation of blood cells, known as red or hematopoietic marrow. As an animal ages, however, much of the marrow is progressively replaced by fat, particularly in the extremities [1]. As a result, active marrow is normally restricted to portions of the axial and proximal appendicular skeleton of the adult. Since much of the axial hematopoietic marrow is difficult to access clinically, most diagnostic sampling in veterinary medicine is limited to a few accessible sites within the appendicular portion of the distribution.

Compared to most tissues, hematopoietic marrow is particularly sensitive to radiation toxicity. Doses as low as 2-4 Gy have been shown to be capable of producing reductions of both cellularity [2] and proliferation [3]. Fractionated doses beyond 30Gy generally produce permanent ablation [4], but a local fractionated dose of only 18Gy was sufficient to produce longstanding cell death in the adjacent vertebral marrow of a dog receiving intensity-modulated radiation therapy (IMRT) for a primary lung tumor (the lung mass itself received a fractionated total dose of 30Gy as a palliative therapy protocol) [5]. Although the ultimate clinical impact of bone marrow suppression also

depends on volume, the concurrent use of chemotherapy and/or the potential to expose rather large areas of bone marrow to lower radiation doses with techniques like IMRT make detailed knowledge of marrow distribution an important consideration in radiotherapy planning [6].

To date, there are few reports that provide specific information about the overall skeletal distribution of canine hematopoietic marrow, and most available data are several decades old. Existing canine functional marrow distribution data have been based on the uptake of ^{59}Fe and ^{99m}Tc-sulfur colloid by erythroid precursors and reticuloendothelial cells, respectively [7]. Additionally, local cellularity estimates have been provided based on microscopic examinations of samples collected from several sites throughout the skeleton of euthanized animals [8]. Unfortunately, both studies appear to be based on relatively young animals; as a result, it is not clear whether their results accurately reflect marrow distribution in the mature dog.

Today, positron emission tomography combined with computed tomography (PET/CT) offers a state-of-the-art method to image and quantify whole-body bone marrow activity. Compared to other modern techniques like magnetic resonance imaging (MRI), which provides an anatomical approach to imaging marrow distribution based largely on its relative fat and water content [9], PET/CT more directly interrogates marrow function by exploiting specific physiologic pathways that mediate the distribution of certain positron-emitting radiopharmaceuticals. In particular, PET/CT using 3'-deoxy-3'-[^{18}F]fluorothymidine (^{18}FLT) has gained attention in recent years as a powerful tool to analyze marrow proliferation [5, 6, 10-15]. As a substrate for the pyrimidine salvage

pathway of DNA synthesis, ^{18}FLT enters proliferating cells and becomes trapped due to phosphorylation by thymidine kinase 1 (TK1) [16-18]. Although it is not subsequently incorporated into DNA, TK1 expression is tightly regulated to the synthetic phase of the cell cycle, and ^{18}FLT retention in various tumors has generally correlated well with traditional assessments of cellular proliferation [18-24]. Since the salvage pathway is particularly robust in hematopoietic marrow due to the recovery of DNA liberated by red blood cell enucleation [25], ^{18}FLT-PET/CT is especially well-suited for assessing the distribution of proliferating marrow.

Using existing whole-body ^{18}FLT-PET/CT scans from normal dogs, the present study seeks to analyze uptake within the marrow compartment to quantify the relative distribution of active marrow throughout the skeleton by anatomical site. This information will provide updated distribution data for the adult dog, and may be used to improve bone marrow sparing efforts during radiotherapy planning or to inform clinical selection of sampling sites for aspirates and biopsies.

Methods

^{18}FLT-PET/CT scans from six adult, University of Tennessee-maintained, research dogs were utilized to gather data on proliferative bone marrow distribution. The dogs that were imaged ranged in age from 3 to 6 years (mean = 4.67 years), weighed between 15.45 kg and 25.91 kg (mean = 19.09 kg), and included one intact male, one castrated male, and four spayed females. Routine history records as well as results of physical examination, hematology, clinical chemistry panels, and whole-body CT imaging were evaluated to verify that the animals had no underlying adverse health conditions.

Scans were performed in ventral recumbency under general anesthesia 77.10 ± 12.83 minutes (mean±SD) following intravenous injection of either 146.34 ± 0.26 MBq ^{18}FLT (mean ± SD; 2 animals) or 66.88 ± 9.98 MBq ^{18}FLT (mean±SD; 4 animals). The ^{18}FLT injected was produced on-site by the radiochemistry laboratory of the Molecular Imaging and Translational Research Program at the University of Tennessee Graduate School of Medicine and was verified by HPLC to be >99% radiochemically pure. The scans were produced on a Biograph mCT (Siemens Medical Solutions USA, Inc., Knoxville, TN) which combines a 64-slice helical CT scanner with a high resolution LSO PET scanner within a single housing. CT and PET imaging were performed in sequence with no alteration in subject positioning. CT scans were performed at 120 kV and 150 mAs with Care Dose™ using a 0.8 pitch and 0.6 mm acquisition slice width but were reconstructed using 2.5 mm slice thicknesses for image analysis. PET imaging was performed over 9-11 bed positions in order to encompass the entire body of the dogs and immediately followed completion of the CT scan. Each bed position was imaged over 3 minutes with an energy acceptance window of 435-650 keV. PET reconstruction utilized CT data for attenuation correction and was performed using the TrueX algorithm (Siemens Medical Solutions USA, Inc., Knoxville, TN) with 3 iterations and 12 subsets resulting in a reconstructed pixel size of 4.07 mm x 4.07 mm. Data was normalized and corrected for dead time, scatter, and radioactive decay.

Regions of interest (ROIs) encompassing 11 separate skeletal sites (skull, cervical spine, thoracic spine, lumbar spine, sacrum, ribs, sternum, scapulae, proximal humeri, ossa coxarum, and proximal femora) were defined by a veterinarian trained in molecular imaging analysis using dedicated analysis software (Inveon Research Workplace v3.0,

Siemens Medical Solutions USA, Inc., Knoxville, TN). For each skeletal region, a 3-dimensional ROI was initially drawn using CT image data with care taken to precisely follow anatomical boundaries in all image planes. Once the ROI was confirmed to encompass the entire skeletal region and exclude neighboring skeletal sites, co-registered PET data were utilized to tailor the ROI based on standardized uptake value (SUV). A minimum SUV threshold of 2.0 was employed to limit the ROI to bone marrow activity and exclude counts from surrounding tissues (a representative image of thresholded vertebral ROIs is depicted in Figure 3.1). Tracer activity was measured within each thresholded ROI and divided by total skeletal activity to derive the percent of active marrow within each skeletal site.

Results

The relative percentage of proliferative bone marrow by anatomical region is organized in Table 3.1 and illustrated in Figure 3.2. The measured mean ± standard deviation percentage of active marrow by skeletal site was 5.74 ± 1.08 for the scapulae, 10.10 ± 3.81 for the humeri, 3.98 ± 1.80 for the femora, 6.76 ± 1.03 for the ossa coxarum, 4.08 ± 0.68 for the sacrum, 19.65 ± 2.27 for the lumbar spine, 32.08 ± 3.72 for the thoracic spine, 9.59 ± 2.11 for the cervical spine, 0.22 ± 0.19 for the skull, 2.67 ± 1.00 for the sternum, and 5.14 ± 2.10 for the ribs. Percentages listed for bilateral structures are summed.

Appendicular proliferative marrow did not extend beyond the proximal aspects of the humeri or femora in any of the scans included in this study. Marrow activity within the skull was minimal and concentrated caudally. Vertebral activity, which represented the

majority of active marrow measured, was predominately within vertebral bodies; however, some activity extended into several larger vertebral processes. A 3-dimensional image of skeletal marrow activity is depicted in Figure 3.3.

Discussion

The relative skeletal distribution of proliferating marrow determined by ^{18}FLT-PET/CT reflects what would be expected in an adult animal, with the bulk of marrow activity concentrated along the axis of the trunk and adjacent limb bones. When compared with the previous description by Greenberg et al [7], several similarities are observed. Notably, the relative distribution based on ^{18}FLT uptake was within approximately 2 percent of the previous estimates determined by both ^{59}Fe and ^{99m}TC-sulfur colloid for the scapulae, humeri, sacrum, skull, and sternum. Further, all three methods indicate that around 10 percent of total skeletal marrow activity lies within the proximal aspect of the humerus, one of the most commonly and easily accessible marrow sampling sites in veterinary species. Relative distribution was somewhat lower in other common sampling sites, such as the iliac crest and proximal femur, suggesting that sampling from the proximal humerus might be preferable in the dog. Larger differences were observed for other sites, with distribution comparatively biased toward the vertebral column and away from the ossa coxarum, femora, and ribs of the animals included in the present study. The disparity was most conspicuous in the measurements of the ribs and thoracic spine, where estimates using ^{18}FLT were approximately 15 percent lower or higher, respectively.

Despite a paucity of information about marrow conversion age with respect to specific skeletal sites in the dog, MRI studies suggest that conversion in the distal femur likely occurs between 1 and 3 years of age [26-29]. Although age was not reported in the Greenberg study [7], marrow activity was described in the distal femora and proximal tibiae. It is therefore probable that the animals used were somewhat younger than those described herein and may have still been undergoing marrow conversion. All of the dogs imaged by ^{18}FLT were greater than 3 years of age and none displayed similar uptake near the stifle. While this likely explains the differences in femoral measurements, it is unclear the extent to which age-related conversion explains the discrepancies between the measurements of the ribs or the ossa coxarum, a tissue that generally maintains the presence of red marrow despite advanced age [26, 30]. Further studies imaging dogs of progressive ages are needed to define the pattern and timing of marrow conversion in the canine.

Although comparisons between species should be considered with caution, it is interesting to compare the present canine percentages with those determined in humans using similar technology. A 2011 study by Hayman et al [6] used ^{18}FLT-PET/CT scans from 13 human cancer patients to describe relative skeletal distribution of hematopoietic marrow in much the same way as presented herein. While general trends were similar between our measurements of the dog and those of the human, only the mean values for the femoral, scapular, and sternal anatomical sites were within 2 percent of one another. Our results indicate that the dog has a greater percentage of active marrow within the humerus and cervical, thoracic, and lumbar portions of the vertebral column, but a relatively smaller percentage within the skull, sacrum, ribs, and

ossa coxarum. The ribs and clavicles were grouped in the human data, likely explaining some of the difference observed since the canine clavicle is extremely small and was therefore not included in our assessments. Interestingly, the difference measured between the ossa coxarum of the two species was rather large at approximately 18.5 percent (6.76 versus 25.3 percent). It is probable that differences in the anatomical proportions of the various sites explains much of the variation between the two species.

This data has several potential limitations. First, the small sample size consisted of only six scans, all of which were from mixed breed dogs of moderate age. Consequently, analysis was limited to basic descriptive statistics and the ability to examine potential factors which may influence bone marrow distribution, such as sex, breed, or life stage, was limited. ROIs were drawn to exclude adjacent soft tissues and neighboring skeletal sites. As a result, partial volume effects (PVE) may influence activity measurements between adjoining sites or within very small ROIs due to spillover of imaged activity and averaging within voxels. PVE typically occur whenever an object is less than three times the full width at half maximum (FWHM) of the reconstructed image resolution [31]. Influence is likely minimal for most skeletal regions described, but evaluations of relative distribution in narrow or small regions of uptake, like the ribs or skull, may be underestimated due to this effect.

Despite potential limitations, ^{18}FLT-PET/CT provides a robust, whole-body assessment of proliferative activity within the marrow compartment. The relative distribution data reported herein provides a modern estimate of marrow activity by skeletal site for the adult dog based on cellular proliferation. This information should assist planning, both

by radiation oncologists aiming to avoid important sites of proliferative marrow and by clinicians choosing sites that are most likely to yield high quality samples for diagnostic testing.

REFERENCES

1. Gurevitch, O., S. Slavin, and A.G. Feldman, Conversion of red bone marrow into yellow - Cause and mechanisms. Med Hypotheses, 2007. 69(3): p. 531-6.

2. Lehar, T.J., et al., Effect of focal irradiation on human bone marrow. Am J Roentgenol Radium Ther Nucl Med, 1966. 96(1): p. 183-90.

3. Everitt, S., et al., Imaging Cellular Proliferation During Chemo-Radiotherapy: A Pilot Study of Serial ^{18}F-FLT Positron Emission Tomography/Computed Tomography Imaging for Non–Small-Cell Lung Cancer. International Journal of Radiation OncologyBiologyPhysics, 2009. 75(4): p. 1098-1104.

4. Perez, C.A., Principles and practice of radiation oncology. 4th ed. 2004, Philadelphia: Lippincott Williams & Wilkins. xxiii, 2527 p.

5. Ballegeer, E.A., et al., Pet/Ct Following Intensity-Modulated Radiation Therapy for Primary Lung Tumor in a Dog. Veterinary Radiology & Ultrasound, 2006. 47(2): p. 228-233.

6. Hayman, J.A., et al., Distribution of proliferating bone marrow in adult cancer patients determined using FLT-PET imaging. Int J Radiat Oncol Biol Phys, 2011. 79(3): p. 847-52.

7. Greenberg, M.L., H.L. Atkins, and L.M. Schiffer, Erythropoietic and reticuloendothelial function in bone marrow in dogs. Science, 1966. 152(3721): p. 526-8.

8. Calvo, W., et al., Regeneration of blood-forming organs after autologous leukocyte transfusion in lethally irradiated dogs. I. Distribution and cellularity of the bone marrow in normal dogs. Blood, 1975. 46(3): p. 453-7.

9. Sebag, G.H., et al., Pediatric spinal bone marrow: assessment of normal age-related changes in the MRI appearance. Pediatr Radiol, 1993. 23(7): p. 515-8.

10. Agool, A., et al., ^{18}F-FLT PET in hematologic disorders: a novel technique to analyze the bone marrow compartment. J Nucl Med, 2006. 47(10): p. 1592-8.

11. Agool, A., et al., F-18 FLT PET: a noninvasive diagnostic tool for visualization of the bone marrow compartment in patients with aplastic anemia: a pilot study. Clin Nucl Med, 2011. 36(4): p. 286-9.

12. McGuire, S.M., et al., Using [^{18}F]Fluorothymidine Imaged With Positron Emission Tomography to Quantify and Reduce Hematologic Toxicity Due to Chemoradiation Therapy for Pelvic Cancer Patients. Int J Radiat Oncol Biol Phys, 2016.

13. McGuire, S.M., et al., 3'-deoxy-3'-[(1)(8)F]fluorothymidine PET quantification of bone marrow response to radiation dose. Int J Radiat Oncol Biol Phys, 2011. 81(3): p. 888-93.

14. McGuire, S.M., et al., A methodology for incorporating functional bone marrow sparing in IMRT planning for pelvic radiation therapy. Radiother Oncol, 2011. 99(1): p. 49-54.

15. Menda, Y., et al., Investigation of the pharmacokinetics of 3'-deoxy-3'-[^{18}F]fluorothymidine uptake in the bone marrow before and early after initiation of chemoradiation therapy in head and neck cancer. Nucl Med Biol, 2010. 37(4): p. 433-8.

16. Shields, A.F., et al., Imaging proliferation in vivo with [F-18]FLT and positron emission tomography. Nat Med, 1998. 4(11): p. 1334-6.

17. Shields, A.F., et al., Kinetics of 3'-deoxy-3'-[F-18]fluorothymidine uptake and retention in dogs. Mol Imaging Biol, 2002. 4(1): p. 83-9.

18. Salskov, A., et al., FLT: Measuring Tumor Cell Proliferation In Vivo With Positron Emission Tomography and 3′-Deoxy-3′-[^{18}F]Fluorothymidine. Seminars in Nuclear Medicine, 2007. 37(6): p. 429-439.

19. Buck, A.K., et al., Imaging bone and soft tissue tumors with the proliferation marker [^{18}F]fluorodeoxythymidine. Clin Cancer Res, 2008. 14(10): p. 2970-7.

20. Choi, S.J., et al., [^{18}F]3'-deoxy-3'-fluorothymidine PET for the diagnosis and grading of brain tumors. Eur J Nucl Med Mol Imaging, 2005. 32(6): p. 653-9.

21. Kenny, L.M., et al., Quantification of cellular proliferation in tumor and normal tissues of patients with breast cancer by [^{18}F]fluorothymidine-positron emission tomography imaging: evaluation of analytical methods. Cancer Res, 2005. 65(21): p. 10104-12.

22. Buck, A.K., et al., 3-deoxy-3-[(18)F]fluorothymidine-positron emission tomography for noninvasive assessment of proliferation in pulmonary nodules. Cancer Res, 2002. 62(12): p. 3331-4.

23. Chen, W., et al., Imaging proliferation in brain tumors with ^{18}F-FLT PET: comparison with ^{18}F-FDG. J Nucl Med, 2005. 46(6): p. 945-52.

24. Wagner, M., et al., 3'-[^{18}F]fluoro-3'-deoxythymidine ([^{18}F]-FLT) as positron emission tomography tracer for imaging proliferation in a murine B-Cell lymphoma model and in the human disease. Cancer Res, 2003. 63(10): p. 2681-7.

25. Muzi, M., et al., Kinetic analysis of 3'-deoxy-3'-fluorothymidine PET studies: validation studies in patients with lung cancer. J Nucl Med, 2005. 46(2): p. 274-82.

26. Armbrust, L.J., et al., Low-field magnetic resonance imaging of bone marrow in the lumbar spine, pelvis, and femur in the adult dog. Vet Radiol Ultrasound, 2004. 45(5): p. 393-401.

27. Armbrust, L.J., M. Ostmeyer, and R. McMurphy, Magnetic resonance imaging of bone marrow in the pelvis and femur of young dogs. Vet Radiol Ultrasound, 2008. 49(5): p. 432-7.

28. Konar M, L.J., Age-related changes in MR appearance of normal bone marrow in canine stifle joints. Abstracts from the annual conference of the European association of veterinary diagnostic imaging. Vet Radiol Ultrasound, 2004. 45(6): p. 586-613.

29. Martig, S., et al., MRI characteristics and histology of bone marrow lesions in dogs with experimentally induced osteoarthritis. Vet Radiol Ultrasound, 2007. 48(2): p. 105-12.

30. Ricci, C., et al., Normal age-related patterns of cellular and fatty bone marrow distribution in the axial skeleton: MR imaging study. Radiology, 1990. 177(1): p. 83-8.

31. Soret, M., S.L. Bacharach, and I. Buvat, Partial-volume effect in PET tumor imaging. J Nucl Med, 2007. 48(6): p. 932-45.

APPENDIX

Table 3.1 Percentage of canine total bone marrow activity by skeletal site

Site	Dog 1	Dog 2	Dog 3	Dog 4	Dog 5	Dog 6	Mean ± SD
Scapulae	7.2	4.6	4.6	6.4	5.2	6.4	5.7 ± 1.1
Proximal Humerus	5.5	6.4	12.5	12.2	8.8	15.2	10.1 ± 3.8
Proximal Femur	1.6	3.2	4.2	5.1	3.1	6.8	4.0 ± 1.8
Ossa Coxarum	6.6	6.7	7.4	7.5	4.8	7.4	6.8 ± 1.0
Sacrum	3.5	4.4	5.2	4.2	3.5	3.6	4.1 ± 0.7
Lumbar Spine	21.1	21.4	16.4	19.0	22.2	17.8	19.7 ± 2.3
Thoracic Spine	33.2	37.5	26.9	31.8	33.9	29.2	32.1 ± 3.7
Cervical Spine	11.6	10.5	10.0	5.8	11.0	8.7	9.6 ± 2.1
Skull	0.2	0.1	0.6	0.0	0.2	0.2	0.2 ± 0.2
Sternum	4.2	2.0	3.6	1.7	2.5	2.0	2.7 ± 1.0
Ribs	5.4	3.3	8.5	6.3	4.7	2.7	5.1 ± 2.1

SD = Standard Deviation

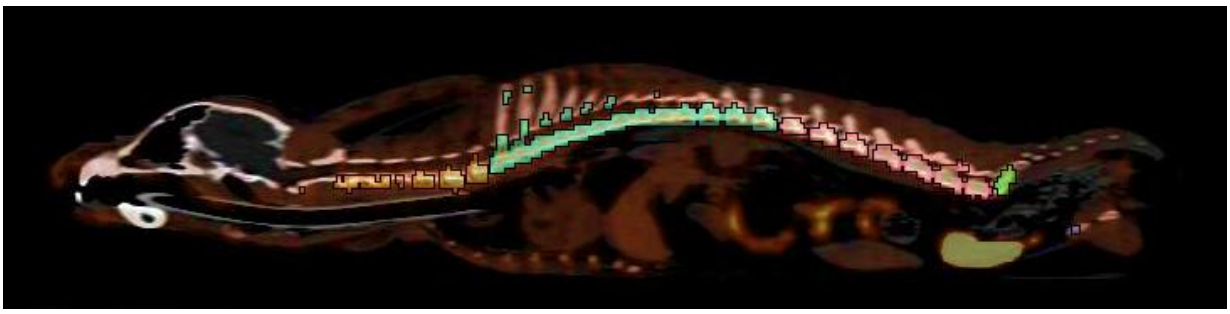

Figure 3.1 Sagittal plane image depicting canine vertebral column regions of interest. Cervical (yellow), thoracic (teal), lumbar (pink), and sacral (green) regions are shown.

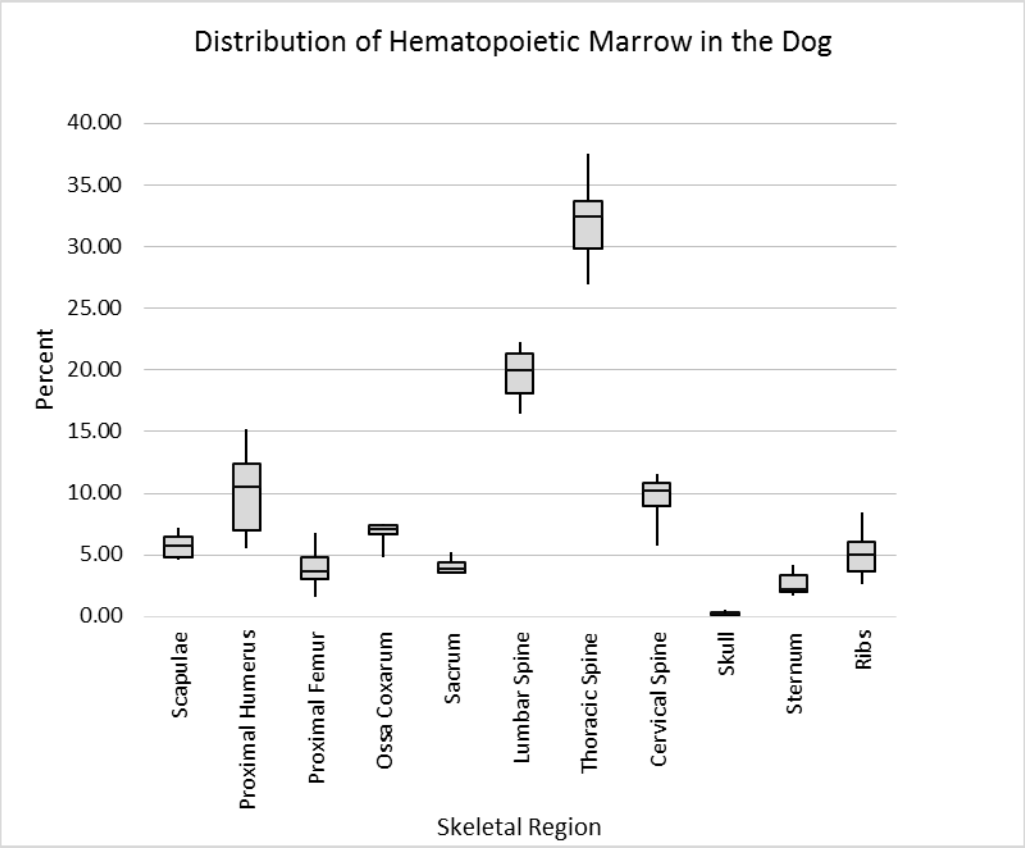

Figure 3.2 Box plots showing percentage distribution of proliferative bone marrow by skeletal site in the adult dog (n = 6).

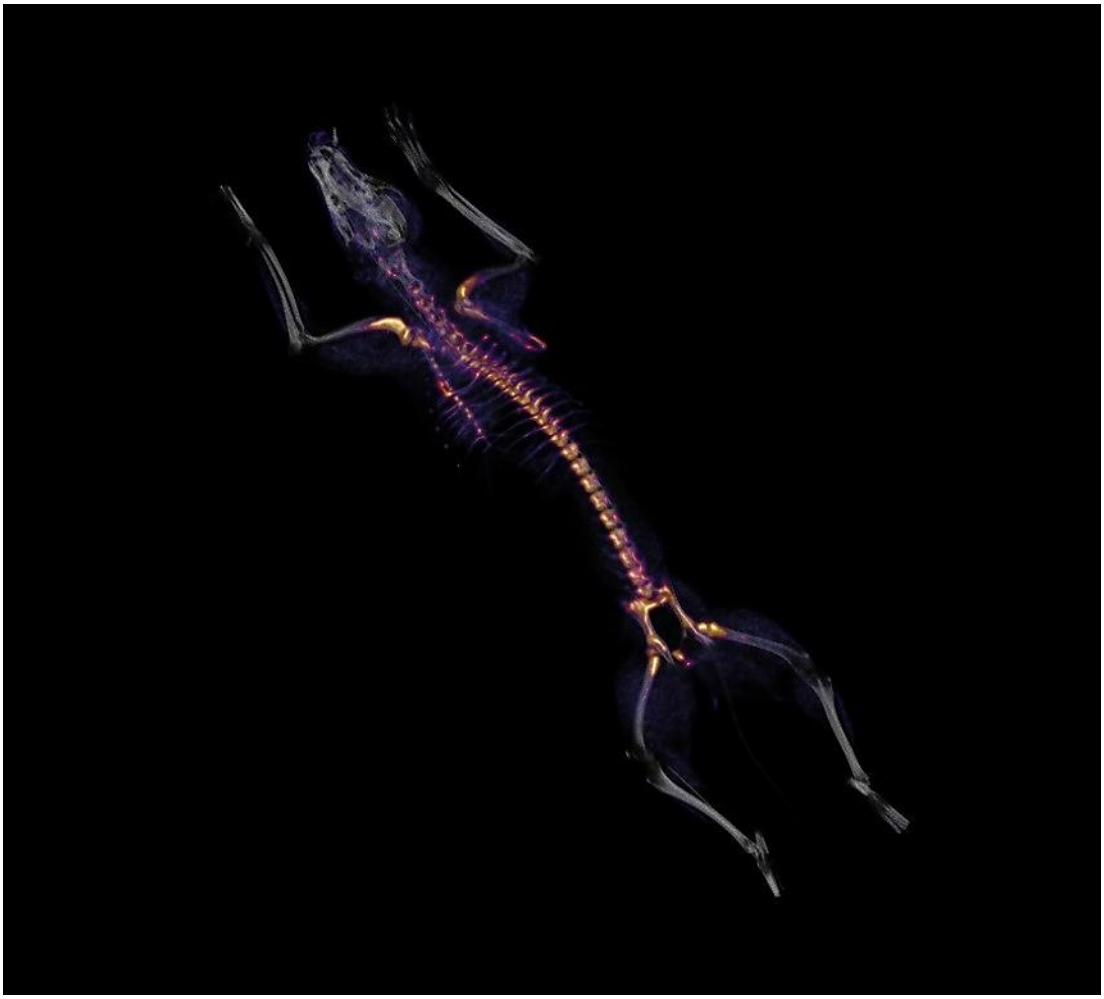

Figure 3.3 Three-dimensionally reconstructed image of canine skeletal marrow activity.

CONCLUSION

The work presented herein documents the normal physiologic distribution of 3'-deoxy-3'-[^{18}F]fluorothymidine (^{18}FLT) in adult dogs and cats. The quantitative measurements included throughout this dissertation may serve as reference values to guide image interpretation in future clinical studies using this tracer to evaluate animals with suspected disease. Observation of similar tracer distribution characteristics in cats, as compared to dogs and humans, validates the first documented use of ^{18}FLT in this species. Although additional studies are needed to define the metabolism of ^{18}FLT in cats and further define that of dogs, positron emission tomography/computed tomography (PET/CT) utilizing ^{18}FLT represents a robust diagnostic tool for noninvasive imaging of proliferative tissues in veterinary patients. As such, the details of normal canine and feline biodistribution will become increasingly relevant as veterinary access to PET and PET/CT continues to grow.

The use of ^{18}FLT-PET/CT to characterize marrow activity has been well defined in human medicine, but this technology has not been used previously for this purpose in veterinary species. Existing descriptions of canine marrow distribution appear to have been based on younger animals that were likely still undergoing marrow conversion. As a result, the present use of ^{18}FLT-PET/CT to evaluate the relative skeletal distribution of proliferating marrow in dogs may represent the only comprehensive whole-body description of the adult pattern of hematopoietic marrow distribution in this species, information that is valuable when selecting diagnostic sampling sites or during radiotherapy planning to minimize hematologic toxicity. Further studies utilizing this technology to define the age-related progression of marrow conversion throughout the skeleton are warranted as such information is limited for veterinary species.

VITA

Joshua Rowe was born in Nashville, Tennessee to his parents, Alan and Janice Rowe. He is the younger of two sons, born about five years after his older brother, Chris. He attended several schools growing up, predominately in Middle Tennessee, before graduating as valedictorian from Franklin County High School in Winchester, Tennessee. During high school, he lived with his father on the family farm, across the field from his grandparents, Howell and Peggy Rowe. It was largely his grandfather, a veteran and a purebred cattle rancher, who initially inspired both his interest in veterinary medicine and his desire to serve his country. He joined the United States Army Reserve at 17 years old, graduating first in his class from the Quartermaster Center and School in Fort Lee, Virginia. While serving in the Army Reserve, he attended the University of Tennessee at Martin, where he studied animal science in preparation for applying to veterinary school. He graduated summa cum laude with a Bachelor of Science degree in Agriculture in December 2005. He then headed to Knoxville, Tennessee where he received his Doctor of Veterinary Medicine degree from the University of Tennessee College of Veterinary Medicine in 2010. While attending veterinary school, he accepted a graduate assistantship in the Comparative and Experimental Medicine Program in pursuit of a career in veterinary education. He graduated with a Doctor of Philosophy degree in December 2017.